

Cosmic Ray Background Rejection with Wire-Cell LArTPC Event Reconstruction in MicroBooNE

MICROBOONE-NOTE-1084-PUB

The MicroBooNE Collaboration*

(Dated: June 20, 2020)

For a large Liquid Argon Time Projection Chamber (LArTPC) operating on or near the surface to detect neutrino interactions, the rejection of cosmic background is a critical and challenging task because of the large cosmic ray flux and the slow timing of the TPC. In this paper, we introduce a superior cosmic background rejection procedure based on the Wire-Cell 3D event reconstruction for LArTPCs. The foundational reconstruction techniques including the 3D imaging and clustering of TPC ionization charge data, processing of PMT light data, and matching of the TPC charge and PMT light information are reviewed. This is followed by a detailed description of track trajectory fitting and dQ/dx determination. These reconstruction tools further enable various methods to tag cosmic-ray muons in time with the neutrino beam spills. From a hardware trigger level 1:20k neutrino to cosmic-ray background ratio, high-performance generic neutrino selection, i.e. cosmic-ray background rejection, is achieved in the MicroBooNE experiment with a cosmic contamination of 14.9% (9.7%) for the visible energy region greater than 0 (200) MeV. High efficiencies of neutrino interactions are also retained, and they are 80.4% and 87.6% for ν_μ charged-current and ν_e charged-current interactions, respectively.

CONTENTS

I. Introduction	1	B. Stopped muon examples	23
II. MicroBooNE detector and readout	3	References	24
III. Review of foundational reconstruction techniques	4		
A. PMT light reconstruction	4		
B. TPC charge reconstruction	4		
1. TPC digital signal processing	5		
2. Tomographic 3D image reconstruction	5		
3. 3D clustering	6		
C. Matching between charge and light	6		
IV. Track trajectory and dQ/dx determination	6		
A. Track trajectory fit	7		
B. dQ/dx fit	8		
C. Performance	9		
V. Rejecting in-beam cosmic-ray backgrounds	10		
A. Effective boundary and fiducial volume	12		
B. Through-going muons (TGM)	12		
C. Stopped muons (STM)	14		
D. Light-mismatched (LM) events	14		
VI. Performance of the generic neutrino detection	16		
VII. Summary and outlook	19		
Acknowledgments	19		
A. Trajectory seed finding	19		

I. INTRODUCTION

The liquid argon time projection chamber [1–4] (LArTPC) is a three-dimensional tracking calorimeter that is widely used in neutrino physics [5–12]. When charged particles traverse the LAr detection medium, ionization electrons and scintillation photons are produced. The detection of scintillation photons by a light detector (e.g. a photomultiplier) provides the time of the activity. Under the influence of an external electric field, the ionization electrons travel at a constant speed toward the anode plane. The transverse position of ionization electrons can be determined using position-sensitive detectors (e.g. multiple parallel wire planes with different wire orientations as shown in Fig. 1) at the anode. Given the drift velocity, the longitudinal position along the drift field can be calculated from the time delay, or drift time, between the time of the particle activity seen by the light detectors and the arrival time of the ionization electrons at the anode. Together, a 3D image of the particle activities with a millimeter-scale position resolution can be achieved. In addition, the number of measured ionization electrons is proportional to the energy deposition of the charged particle, which can provide particle identification (PID) information.

Compared to the water Cherenkov or liquid-scintillator detector technology, the LArTPC is expected to have a higher efficiency in differentiating electrons from gamma rays in neutrino interactions through gap identification and dE/dx measurement [13]. Such a capability allows an excellent detection of ν_e charge-current interactions, which enables precision measurements of $\bar{\nu}_\mu \rightarrow \bar{\nu}_e$ os-

* MICROBOONE_INFO@fnal.gov

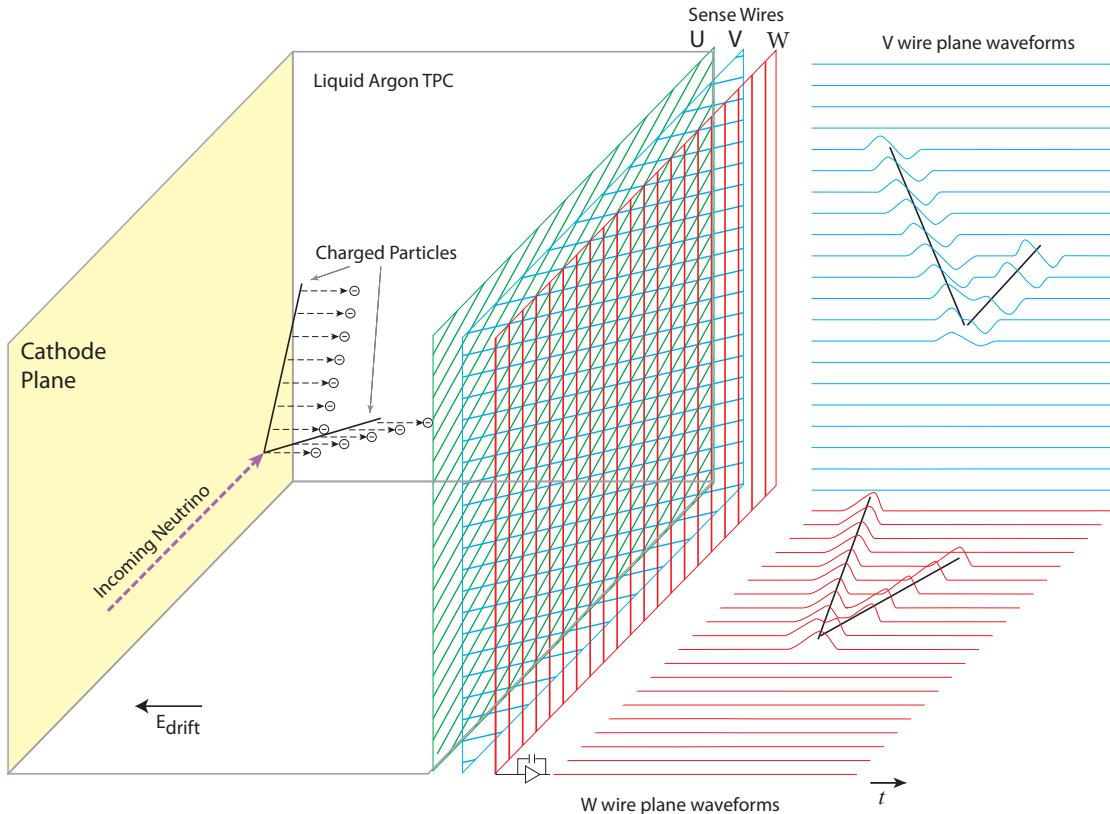


FIG. 1. Illustration of a LArTPC detector. Taken from Ref. [7].

cillations. Utilizing the LArTPC technology, the MicroBooNE experiment [7] aims to understand the nature of the low-energy excess of ν_e -like events observed in the MiniBooNE experiment [14] and to measure neutrino-argon interaction cross sections [15, 16]. The Short Baseline Neutrino (SBN) Program [17], consisting of three large LArTPCs on the surface, is under construction to search for light sterile neutrinos [18]. Moreover, the Deep Underground Neutrino Experiment (DUNE) [19], with $\sim 10,000$ m³ detector modules, is planned to search for CP violation in leptons [20] and to determine the neutrino mass ordering [21]. To ensure the success of these current and future physics programs, the current-generation large LArTPCs operating on the surface, such as MicroBooNE [7] and ProtoDUNE [12], are critical in developing and demonstrating the full capability of this technology.

For LArTPCs operating on the surface, the presence of cosmic ray muons occurring at a rate of $\sim 0.2/\text{m}^2/\text{ms}$ is a major challenge to efficiently reconstructing neutrino interactions, the rate of which is generally several orders of magnitude smaller. This challenge is the result of the

slow timing of the TPC (typical readout time of a few ms), and the decoupling of the ionization charge and scintillation light signals, since they are measured by separate detectors. In this paper, we present a high-performance neutrino detection (or cosmic background rejection) procedure based on the Wire-Cell LArTPC event reconstruction techniques [22] in the MicroBooNE experiment.

The MicroBooNE detector [7] consists of a $2.56 \text{ m} \times 2.32 \text{ m} \times 10.36 \text{ m}$ (~ 85 metric tons of LAr) active TPC for ionization charge detection and an array of 32 photomultiplier tubes (PMTs) [23] for scintillation light detection. It is located along the Booster Neutrino Beam (BNB) [24] of the Fermi National Accelerator Laboratory (FNAL) in Batavia, IL. Sitting on the beam axis, 463 m from the beam target, MicroBooNE observes one neutrino interaction inside the TPC active volume per ~ 680 spills at the nominal beam intensity of 4.25×10^{12} protons on target (POT) per pulse. Each proton pulse is called a spill, and lasts $1.6 \mu\text{s}$. When the BNB delivers a beam spill, a hardware trigger is initiated in MicroBooNE, which results in the recording of 4.8 ms of TPC data and $23.4 \mu\text{s}$ of PMT data covering the beam spill

window. This record is referred to as an event. In addition, self-discriminated PMT readouts are taken during a period of 6.4 ms around the BNB trigger. Section II provides more details about the MicroBooNE detector and its readout.

To reduce data size, a software trigger requiring significant PMT signals to be coincident with the beam spill is applied in data acquisition (DAQ) to decide whether to keep an event or not. After rejecting those events with low light output, therefore making them incompatible with particle activity from beam neutrino interactions, a data reduction by a factor of 22 is achieved. Still, after the software trigger, over 95% of the remaining events have only cosmic rays within the trigger window. Furthermore, at the rate of 5.5 kHz [25], there are on average 26 cosmic-ray muons in the full 4.8 ms readout window. Such an overwhelming amount of cosmic rays creates significant challenges in selecting neutrino events [16, 26–28]. In this work, an offline light reconstruction is first applied to reject events triggered by cosmic rays arriving just before the beam spill, leading to a factor of 4 reduction of triggered events. Then, a novel TPC-charge to PMT-light matching algorithm, which requires digital signal processing of the TPC data followed by the reconstruction of 3D images and activity clustering, is applied to remove TPC activity from cosmic rays outside of the beam spill. Section III briefly summarizes these techniques. The rejection of stopped muons requires a new set of tools to reconstruct the particle track trajectory and its dQ/dx , which is described in detail in Sec. IV. The rejection of the remaining background dominated by cosmic rays in coincidence with the beam spill is described in Sec. V. In particular, the rejection of through-going muons based on geometry information, the rejection of stopped muons based on the rise in reconstructed ionization charge per unit distance (dQ/dx) near the candidate stopping point, and the re-examination of mismatched charge-light pairs are described in Sec. VB, Sec. VC, and Sec. VD, respectively. The final performance of this procedure on cosmic ray rejection and neutrino detection is shown in Sec. VI before the summary in Sec. VII.

II. MICROBOONE DETECTOR AND READOUT

The MicroBooNE detector [7] is a large LArTPC designed to observe neutrino interactions from the on-axis BNB [24] and the off-axis NuMI [29] neutrino beam at FNAL. Figure 2a shows the MicroBooNE TPC that is housed in a foam-insulated evacuable cryostat vessel.

As shown in Figure 2b, the cathode plane high voltage is set at -70 kV during the normal operation, leading to a drift field of 273 V/cm. In this field, the ionization electrons drift at a speed of 1.1 mm/ μ s [31], corresponding to a 2.3 ms drift time for the maximum 2.56 m

drift distance. At the anode side, there are three parallel wire readout planes (see Figure 1). In the drift direction, these planes are labeled as the “U”, “V”, and “W” planes, with each plane containing 2400, 2400, and 3456 wires, respectively. The wire spacing within a plane is 3 mm, and the planes are spaced 3 mm apart. The wires in the W plane run vertically and the wires in the U and V planes are oriented $\pm 60^\circ$ with respect to the vertical direction. Different orientations of the wires allow for determination of transverse positions of the ionization electrons with respect to their drift direction. Bias voltages for the U, V, and W planes are -110 V, 0 V, and 230 V, respectively, which satisfies the transparency condition so that all drifting electrons pass through the U and V (induction) wire planes and are fully collected on the W (collection) plane. As the ionization electrons approach a wire plane, the induced current on each wire is amplified, shaped, and digitized through a custom designed CMOS analog front-end ASIC [32] operating at 87 K in the liquid argon. The direct implementation of readout electronics in the cold liquid leads to a significantly reduced electronics noise. The equivalent noise charge (ENC) on each wire is generally below 400 electrons [33].

Figure 2b also shows the light collection system behind the anode wire planes. Thirty-two 8-inch Hamamatsu R5912-02MOD PMTs [23], providing approximately uniform coverage in the anode plane, are used to detect scintillation light from the LAr and provide the start time of particle activity. A tetraphenyl butadiene (TPB) coated plate is installed in front of each PMT to shift the wavelength of argon scintillation light from ultraviolet to the visible part of the spectrum to which the PMT is sensitive. Each PMT is operated with a positive bias voltage, and the signal from the high voltage line is split into two separated readouts with different gains (a low gain of $\times 1$ and a high gain of $\times 10$). The two readouts are merged offline and the overall dynamic range is enhanced. The magnitude of the detected light on each PMT (i.e. the light pattern) provides information regarding the position of time-isolated particle activities, which can be compared with the predicted light pattern from the ionization charge signals. A successful match determines the association between individual TPC activity and light detection, and therefore the time of the corresponding TPC activity. In Sec. IIIC, we describe an algorithm that significantly improved this charge-light matching performance.

Each event in MicroBooNE consists of data from both the TPC and the PMT data. The DAQ readout window for the TPC is 4.8 ms in duration spanning from -1.6 ms to +3.2 ms relative to the trigger time. This time duration is slightly more than twice the time needed for an ionization electron to drift across the full width of the detector (2.3 ms). At the digitization frequency of 2 MHz, 9600 samples (or time ticks) of the waveform from each wire channel is recorded. There are a total of 8256 wire channels. For the PMT data, there are two separated

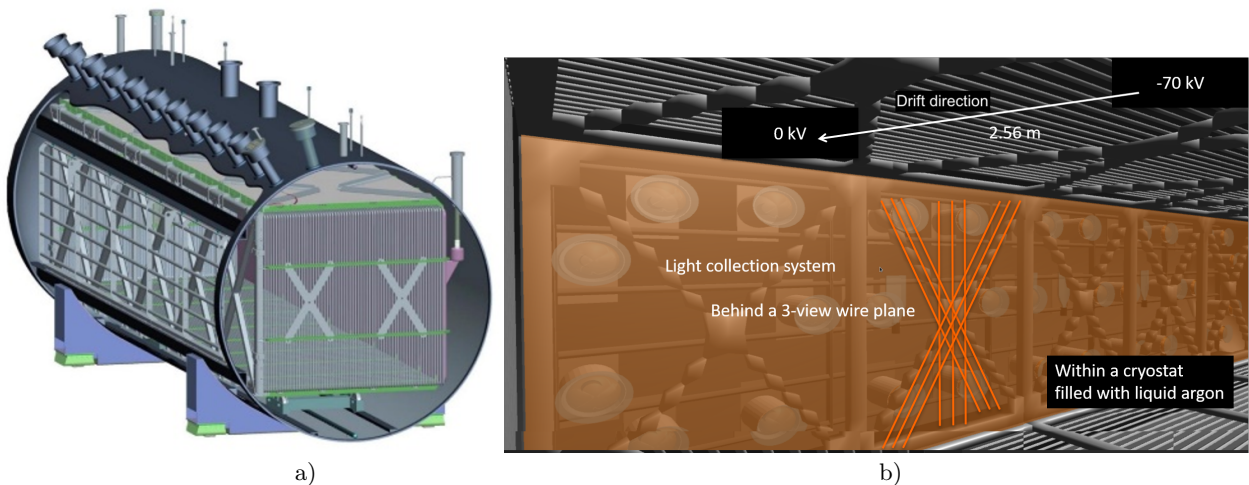


FIG. 2. (Left) The cryostat of the MicroBooNE detector. The field cage is shown inside the cryostat. (Right) Inside the cryostat of the MicroBooNE detector, visualized with the VENU software [30]. The maximum drift distance is 2.56 m with a drifting electric field of 273 V/cm. The light collection system of 32 PMTs is behind the ionization charge detection system of three parallel anode wire planes.

trigger streams. Within each event, 1500 samples (digitized at 64 MHz) covering the beam spill are recorded for every PMT channel, which is referred to as the *beam discriminator*. In addition, self-discriminated PMT readouts, each with 40 samples, are taken during a period of 6.4 ms around the trigger time in order to record the cosmic activity that may enter the beam activity frame because of the relatively slow drift of ionization electrons. They are referred to as the *cosmic discriminator*.

III. REVIEW OF FOUNDATIONAL RECONSTRUCTION TECHNIQUES

This section describes some foundational reconstruction techniques for the TPC and PMT data implemented in the Wire-Cell reconstruction for the LArTPC. Since most of these techniques have been reported in detail elsewhere, they are briefly summarized for the completeness of this paper.

A. PMT light reconstruction

The PMT waveforms are processed offline to reconstruct a flash, which is a cluster of PMT signals close in time. For the cosmic discriminator (40 samples), the photoelectrons (PEs) are calculated by integrating over a certain time window after the baseline (estimated from the first sample) is subtracted¹. A flash is then formed by

requiring a 100 ns coincidence window among all PMTs, which takes into account the intrinsic light flight time and the timing difference of the PMTs. For the beam discriminator (1500 samples), a deconvolution using Fast Fourier Transformation (FFT) is performed to remove the RC-CR⁴ and RC responses from the signal shaper and the splitter, respectively. A flash is then formed if it satisfies the requirements of multiplicity (>2 with a threshold of 1.5 PE) and total PE (>6) in a 100 ns window. Unless another flash is found in the following microseconds, a flash lasts 7.3 μ s in order to properly include the contribution from the late scintillation light and to exclude the effect from excess noise. The time bin with the maximum PE marks the time of the flash. When the beam discriminator data is present, the data from the cosmic discriminator is ignored. With this offline light reconstruction, 32% of the BNB events from the software trigger remain after requiring the time coincidence of the flash with the beam spill. The flash corresponding to the beam discriminator is shown in the zoomed-in region near 4 μ s. More details of the PMT light data processing can be found in Ref. [34].

B. TPC charge reconstruction

distinct with a much shorter RC time constant, the calculation of PE relies on the peak height after the baseline subtraction instead of the integral.

¹ For one particular PMT where the electronics response is clearly

1. TPC digital signal processing

The first stage of the TPC charge data reconstruction includes noise filtering [33] and signal processing [35, 36]. The noise filtering step removes the excess noise on the wire channels, including noise from the high-voltage power supply for the cathode plane through identifying spikes in the frequency domain, and the removal of noise from the low-voltage regulator for the cold electronics through a coherent noise subtraction in the time domain. In addition, about 10% non-functional channels are identified on an event-by-event basis. More details can be found in Ref. [33]. After noise filtering, the TPC signal processing step reconstructs the ionization charge distribution from the digitized wire channel waveforms. The overall impulse response function includes the field response that describes the induced current from a moving charge in the TPC and the electronics response that characterizes the amplification and shaping of the induced current. Since this function does not depend on the absolute time and position of the ionization electron cloud, a deconvolution technique using a FFT can be used. Compared to the one-dimensional deconvolution [37] used in previous work, the signal processing in this work adopts a novel 2D deconvolution technique [35], which significantly improves the performance of the two induction wire planes. As a result, the deconvoluted waveforms from three wire planes are demonstrated to be matched both in their magnitudes and in their shapes. The TPC signal also shows good agreement between data and the improved TPC simulation, which takes into account the long-range and fine-grained position-dependent field response functions [36].

2. Tomographic 3D image reconstruction

The signals on the three wire planes provide three co-axial projective views of particle activities in the TPC. The three reconstructed 2D (time vs. wire) ionization charge distributions are then fed into a novel tomographic 3D image reconstruction algorithm: Wire-Cell [22], which consists of the following steps:

Geometric tiling: Along the drift direction, a 2D cross-sectional image is reconstructed within every $2 \mu\text{s}$ time slice in a tiling procedure. In each cross-sectional image, the continuously fired wires are merged to form a wire bundle. Regions called blobs representing the overlapping area of these wire bundles from each of the three views within the time slice are created. A blob is therefore the geometric unit in the Wire-Cell reconstructed 3D image. The resulting image represents the most exclusive possibility that is geometrically compatible with the measurements.

Charge solving: Under the assumption that the same amount of ionization charge is seen by each (induction or collection) wire plane, linear equations connecting the

unknown true charges of the blobs and the measured charges on wires can be constructed. Naturally, spurious blobs will have zero charge after solving the equations and can be removed from the image. On the other hand, in many occasions the linear equations are under-determined, which is the result of loss of information from $O(n^2)$ pixels to $O(n)$ wire measurements in each 2D image. In those cases, constraints from the sparsity, non-negativity, and connectivity information are used to solve the equations using the Compressed Sensing technique [38].

3D imaging: The 3D image of the event is then reconstructed by simply concatenating all the 2D cross-sectional images in the time dimension. A natural by-product of the Wire-Cell 3D image reconstruction is the 3D charge of each blob, which plays a crucial role in the charge-light matching as will be described in Sec. III B 3.

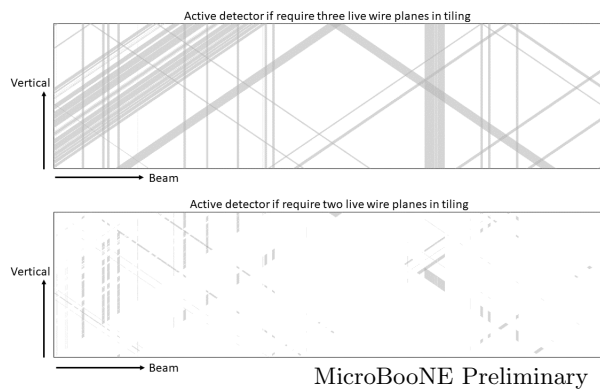


FIG. 3. (Top) The dead regions in the Y-Z plane in gray when requiring all 3 planes to be functional. (Bottom) The dead regions in the Y-Z plane in gray when requiring 2 out of 3 planes to be functional. The Wire-Cell 3D image reconstruction allows tiling with only two live planes, which reduces the dead region percentage from $\sim 30\%$ (top panel) to $\sim 3\%$ (bottom panel).

In MicroBooNE, due to the existence of $\sim 10\%$ non-functional channels, a 3D image reconstruction requiring all three wire planes to be live would yield about 30% non-functional volume, as shown in the top panel of Figure 3. Instead, an alternative procedure requiring only two live planes is developed (with the wires in the third plane allowed to be either fired or non-functional). This reduces the non-functional volume to $\sim 3\%$, as shown in the bottom panel of Figure 3, at the cost of increasing number of spurious blobs. Additional algorithms such as iterative reconstruction and de-ghosting are implemented to improve the quality of the 3D event images. Since the Wire-Cell 3D image reconstruction only uses very general constraints, the reconstruction of the event is independent of its topology (e.g. tracks or electromagnetic showers). More details can be found in Ref. [34].

3. 3D clustering

The reconstructed 3D image consists of thousands of blobs for a typical BNB event. It is important to further group them into clusters, so that each cluster can represent activity from individual cosmic ray or neutrino interactions. Since a LArTPC is a fully active detector, tracks from a charged particle are expected to leave continuous energy depositions, which leads to connected blobs in the 3D image. Therefore, a set of 3D clustering algorithms based on 3D proximity and directionality is created. The use of 3D directionality is necessary to cluster electromagnetic showers together.

Special algorithms are implemented to deal with gaps in the 3D image. A gap could result from the 3% non-functional volume due to the 10% non-functional channels, inefficiency introduced by the coherent noise removal step in the noise filtering [33], or inefficiency introduced by the signal processing step for the prolonged track topology [35] where the TPC signals are typically longer than tens of μs . In addition, coincidental overlap could happen when ionization charge produced at different times and different TPC locations (e.g. from two muons) arrives at the anode plane at the same time and position. This leads to two separated clusters being identified as a single one. A special algorithm is created to separate such merged clusters assuming they follow a long-track-like topology. More details of the 3D clustering algorithms can be found in Ref. [34].

C. Matching between charge and light

Compared to other types of tracking calorimeters, such as NO ν A [39], MINER ν A [40], or MINOS [41], in a LArTPC the event topology information (from ionization charge) and the timing information (from scintillation light) are decoupled. In the MicroBooNE detector, within the readout window of 4.8 ms, the typical number of TPC clusters in the active volume is 20–30. On the other hand, the typical number of PMT flashes, which is also sensitive to the activity in LAr outside the active volume, is 40–50. There is no direct association between a charge cluster and a light flash.

A novel many-to-many charge-light matching algorithm is developed to properly find the corresponding PMT flash for every TPC cluster. Instead of matching the reconstructed positions of the light and charge directly, the hypothesis of a pair of TPC cluster and PMT flash is examined. For each hypothesis, the observed PMT light pattern can be compared to the predicted light pattern by assuming that the scintillation light yield is proportional to the reconstructed ionization charge in each 3D voxel [34]. For each cluster-flash pair, since the electron drift start time is assumed to be the PMT flash time other than the default beam-spill time, the position of ionization charge along the drift direction

can be corrected, which in turn determines the light production voxels. This allows the light prediction at each PMT to take into account the light propagation and acceptance as parameterized by a photon library generated by GEANT4. If the prediction matches the measured flash light pattern, the hypothesis is accepted.

All possible hypotheses of pairs of TPC cluster and PMT flash are constructed after taking into account the geometry constraints. For example, if a TPC cluster is not fully contained in the maximum in-time drift window given a PMT flash time, the hypothesis of this pair is not considered. To select the best hypotheses, the Compressed Sensing technique that was used in the 3D image reconstruction (Sec. III B 2) is again adopted, which not only greatly reduces the computational cost, but also naturally takes into account the following different situations:

1. One TPC cluster can match one PMT flash, which is the majority of cases.
2. One TPC cluster can match zero PMT flashes due to the inefficiency in the light detection system, especially for low energy activities near the cathode plane (since the PMTs are behind the anode planes).
3. One PMT flash can match zero TPC clusters because the light system is sensitive to activities outside the TPC active volume.
4. One PMT flash can match multiple TPC clusters if the previous clustering step fails to group the same interaction activities together (i.e. under-clustering).

The average accuracy of the charge-light matching algorithm is about 95%, evaluated both with Monte Carlo simulation (by truth information) and with data (by hand-scan). More details of the matching algorithms and performance can be found in Ref. [34]. After the charge-light matching, the TPC cluster bundle (one or more clusters) that is matched to an in-beam flash becomes a neutrino interaction candidate.

IV. TRACK TRAJECTORY AND dQ/dx DETERMINATION

In the previous section, we summarized existing foundational event reconstruction techniques, which lead to the selection of TPC activity in-time with the beam spill. In this section, we describe a set of new tools used to determine the track trajectory and associated reconstructed charge per unit length (dQ/dx). For generic neutrino detection, these tools are essential in rejecting one of the main remaining background events: stopped muons (STMs). An STM is a muon that entered the active TPC volume in coincidence with the beam spill and stopped inside the active volume. While tracks from a neutrino

interaction originate inside the active volume and travel outward, an STM enters from outside traveling inward, therefore the primary difference is the direction of the track. The direction of a stopped track is best determined by searching for a rise in dQ/dx (often referred to as the Bragg peak) near the candidate stopping point along its trajectory. Multiple Coulomb Scattering (MCS) is another tool to determine a track's direction [42, 43], although it is not used in this work because of the good performance of dQ/dx alone.

To fully realize the tracking and calorimetry capability of the LArTPC, 3D tracking and dQ/dx measurements are performed through a fit comparing a track hypothesis (a set of ordered 3D points with their associated ionization charge) with the three sets of 2D wire plane measurements of the reconstructed ionization charges as a function of the drift time and the wire number.

In principle, a simultaneous fit to track trajectory and dQ/dx can be performed. In practice, the execution of such a fit is computationally challenging because of its non-linear nature. Instead, a two-step fit is adopted, first focusing on the determination of the track trajectory then on the dQ/dx extraction. After decoupling these two problems, the stability of each step is ensured by applying several advanced linear algebra techniques.

A. Track trajectory fit

The goal of the track trajectory fit is to determine a fine-grained 3D trajectory that is consistent with the detector intrinsic position resolution. The final result of the fit is a set of ordered 3D points $S\{x_j, y_j, z_j\}$ for each TPC *cluster*, which when projected onto the three wire planes best matches the measured 2D trajectories: $U\{u_i, t_i\}$, $V\{v_i, t_i\}$ and $W\{w_i, t_i\}$. Note that here we implicitly assume that each cluster is a single track-like object. This simplified assumption is sufficient for most of the cosmic background removal tasks described in this work.

To perform the track trajectory fit, both the 2D images from wire plane measurements after signal processing (Sec. III B 1) and the Wire-Cell 3D imaging results (Sec. III B 2) are used. The Wire-Cell reconstructed 3D image by itself has a coarse resolution because of: 1) diffusion of ionization electrons during their transportation; 2) application of the software filter in signal processing; and 3) the geometric degeneracy for isochronous tracks leading to large blobs. However, the 3D image is important as it provides a base data structure, from which Graph Theory algorithms are extensively used to find the initial seed of the 3D trajectory. The 3D seed is then utilized to associate nearby 2D pixels for the trajectory fit. This preparatory work is crucial for the fitting procedures described below, but mathematically is rather complex, and exhaustive care is taken to deal with the $\sim 10\%$ non-functional channels. Therefore, we leave the details of

the preparatory work to Appendix A.

Since a TPC cluster typically has a limited number of 3D points, rather than use localized Kalman-filter approaches [44], a global track fitting strategy inspired by the Projection Matching Algorithm [45] is adopted. An empirical test statistic T based on a charge-weighted distance is constructed to compare the projected 2D trajectory given a 3D trajectory $S\{x_j, y_j, z_j\}$ with the 2D measurement of each wire plane:

$$T(S\{x_j, y_j, z_j\}) = \sum_{k=U, V, W} T_k, \quad (1)$$

where the index k sums over the U, V, and W wire planes. For instance, for the U plane we have:

$$T_u = \sum_j \sum_i \frac{q_i^2}{\delta q_i^2} \cdot (\Delta L_u)_{ij}^2, \quad (2)$$

$$(\Delta L_u)_{ij}^2 = \Delta u^2 \cdot (u_i - u_j(y_j, z_j))^2 + \Delta x^2 \cdot (t_i - t_j(x_j))^2. \quad (3)$$

Here, j represents the index of each 3D point in the track trajectory to be determined, and i represents the index of a nearby 2D pixel in the data measurement from a wire plane. The association between a 3D point and its nearby 2D pixels is pre-calculated using the initial seed of the track trajectory, so that only a limited number of 2D pixels are included in the fit (Appendix A). ΔL represents the distance between the pixel i and the 2D projection of the associated 3D point j on the trajectory. The 2D coordinates (u_i, t_i) are the wire number and time slice number of pixel i , while (u_j, t_j) are the projected 2D coordinates from the associated 3D point j on the trajectory. The projection from (x_j, y_j, z_j) to (t_j, u_j, v_j, w_j) is calculated as follows:

$$t = \frac{1}{\Delta x} \cdot x + t_0$$

$$u = \frac{1}{\Delta u} \cdot (-\sin(\theta_u)y + \cos(\theta_u)z) + u_0$$

$$v = \frac{1}{\Delta v} \cdot (-\sin(\theta_v)y + \cos(\theta_v)z) + v_0$$

$$w = \frac{1}{\Delta w} \cdot (-\sin(\theta_w)y + \cos(\theta_w)z) + w_0, \quad (4)$$

where Δx , Δu , Δv , Δw are the width of the time slice and wire pitches of the U, V, W plane, respectively. θ_u , θ_v and θ_w are the wire orientations with respect to the vertical direction for each wire plane, and (t_0, u_0, v_0, w_0) are the coordinates of the origin. Finally, q_i and δq_i in Eq. (2) are the deconvolved charge and its associated uncertainty at pixel i . The ratio of the two provides a weight to the distance ΔL , which enhances the contribution of high charge pixels and suppresses the contribution from the pixels with large charge uncertainties. This weighting strategy is particularly necessary given the presence of non-functional channels.

By substituting Eq. (4) and Eq. (2) into Eq. (1), we can rewrite the test statistic T in a compact matrix form:

$$T = \sum_{k=u,v,w} (M_k - R_k \cdot S)^2, \quad (5)$$

where $S\{x_j, y_j, z_j\}$ is a vector representing the 3D trajectory to be determined, M_k is the charge-weighted 2D pixel coordinates and R_k is the charge-weighted projection matrix derived from Eq (4) for each wire plane. The best-fit 3D trajectory S after minimizing T is the solution of the following equation:

$$\left(\sum_{k=u,v,w} R_k^T R_k \right) \cdot S = \left(\sum_{k=u,v,w} R_k^T \cdot M_k \right). \quad (6)$$

In practice, the dimension of the matrix $(\sum_k R_k^T R_k)$ can be very large, and its direct inversion is computationally challenging. Instead, we use the Biconjugate Gradient Stabilized method (BiCGSTAB) [46], which is an iterative method to numerically solve a linear system with fast convergence.

This track trajectory fitting process is iterated twice, first with a coarse spacing (1.2 cm) of the 3D trajectory points, and then again with a fine spacing (0.6 cm). For each iteration, the following procedures are applied in order:

1. The initial 3D trajectory seed is determined with a coarse or fine spacing.
2. The association between the initial 3D seed and a limited number of nearby 2D pixels is formed.
3. The test statistic T as described in Eq. (5) is constructed and the best-fit trajectory points to minimize T are calculated based on Eq. (6).
4. The best-fit trajectory points are evaluated to ensure proper ordering and consistent charge distribution.

The final result is a fine-grained 3D track trajectory that best describes the wire plane measurements, allowing for accurate dQ/dx determination in the next step. Further details of the procedures are described in Appendix A.

B. dQ/dx fit

With the track trajectory $S\{x_j, y_j, z_j\}$ determined previously, the goal of the dQ/dx fit is to assign a charge Q_j , which is proportional to the number of ionized electrons of the associated discrete step, to each 3D trajectory point (x_j, y_j, z_j) . The dQ/dx along the track trajectory can then be trivially calculated. Similar to the track trajectory fit, an empirical test statistic is constructed to

compare the predicted 2D pixel charge, given a 3D charge Q_j , with the 2D charge measurement of each wire plane:

$$T(S\{Q_j\}; S\{x_j, y_j, z_j\}) = \sum_{k=u,v,w} T_k + T_{\text{reg}}, \quad (7)$$

where the index k sums over the U, V, and W wire planes, and T_{reg} is a regularization term. For instance, for the U plane we have:

$$T_u = \sum_i \frac{1}{\delta q_i^2} \cdot \left(q_i - \sum_j R_{ij}^u Q_j \right)^2. \quad (8)$$

where j , i , q_i and δq_i have the same meaning as in Eq. 2.

R_{ij}^k in Eq. (8) is a conversion factor to enable the comparison between the 3D charge Q_j at generation and the measured charge q_i at a wire. In theory, such a conversion involves the entire TPC signal formation and processing chain, which includes: 1) diffusion of the charge cloud Q_j as it travels toward the anode plane; 2) induced current on the sensing wires due to the TPC field response; 3) amplification and shaping of the current due to the electronics response; and 4) digital signal processing to remove noise and deconvolve the induced signal back to the number of electrons. In practice, this chain of processes is computationally inhibiting to be directly included in the fit. Instead, an effective signal formation model based on the Gaussian approximation is used. In this model, the diffusion coefficients D_L and D_T for the longitudinal (along the E-field) and transverse (perpendicular to the E-field) directions are assumed to be 6.4 and 9.8 cm²/s, respectively [31]. Since the interaction time t_0 of the TPC cluster has been determined during charge-light matching step [34], the broadening of the charge cloud due to diffusion can be predicted as:

$$\sigma_{D_L} = \sqrt{2D_L \cdot t_{\text{drift}}}, \quad \sigma_{D_T} = \sqrt{2D_T \cdot t_{\text{drift}}}, \quad (9)$$

with t_{drift} being the overall drift time. Additional broadening of the reconstructed charge comes from the software filters during signal processing. This broadening is approximated as $\sigma_{F_t} = 1.57$ mm, $\sigma_{F_u} = 0.36$ mm, $\sigma_{F_v} = 0.60$ mm, and $\sigma_{F_w} = 0.11$ mm, for the drift direction, induction U plane, induction V plane, and collection W plane, respectively. These broadening widths are added in quadrature for each wire plane to produce the final width of the Gaussian smearing in the effective model, from which R_{ij}^k in Eq. 8 is calculated.

Finally, T_{reg} in Eq. (7) is a regularization term that incorporates the smoothness of the dQ/dx curve along the track trajectory into the fit. It is defined as:

$$T_{\text{reg}} = \sum_i \left(\sum_j F_{ij} \cdot \frac{Q_j}{s_j} \right)^2, \quad (10)$$

where s_j represents the length of the j th segment, which is taken as the average distance between point j and its

previous and next points, i.e. $s_j = (|\vec{r}_j - \vec{r}_{j-1}| + |\vec{r}_j - \vec{r}_{j+1}|)/2$. Effectively, Q_j/s_j represents the dQ/dx for the 3D trajectory point j . F is the regularization matrix with the following format:

$$F = \eta \cdot \begin{bmatrix} -1 & 1 & 0 & \dots & 0 & 0 & 0 \\ 1 & -2 & 1 & \dots & 0 & 0 & 0 \\ \vdots & \vdots & \vdots & \ddots & \vdots & \vdots & \vdots \\ 0 & 0 & 0 & \dots & 1 & -2 & 1 \\ 0 & 0 & 0 & \dots & 0 & 1 & -1 \end{bmatrix}, \quad (11)$$

where η is the regularization strength. The regularization term effectively calculates the overall second-order derivative of the Q_j/s_j curve, and penalizes those points with large local curvatures. This term is important in the dQ/dx fit to mitigate the impact of ill-defined points, especially when the 2D pixels are inside or close to the non-functional channels. The regularization strength η is set to be 0.3 or 0.9 if the non-functional channels belong to induction or collection wire planes, respectively. Further adjustment to η is made for each trajectory point j if the adjacent points share a large number of nearby 2D pixels.

With the test statistic T defined in Eq. (7), the best-fit set of charge depositions $S\{Q_j\}$ for all 3D trajectory points can be obtained by minimizing T with respect to Q_j . Since the trajectory itself is fixed in the previous step (Sec. IV A), the minimization of T leads to a system of linear equations similar to those in Eq. (6) and can be solved numerically using the BiCGSTAB method [46] when the dimension is high. Reducing the problem to a linear system significantly improves the stability and the speed of the fit. Finally, as defined in Eq. (10), dQ/dx for each point j is calculated as the ratio between Q_j and its corresponding segment length s_j .

Accurate determination of track trajectory and dQ/dx is key to rejecting many of the cosmic ray backgrounds described in this work and plays a central role in future work such as performing particle identification. Figure 4 shows the performance of dQ/dx determination for a simulated muon track. The reconstructed dQ/dx is consistent with the true dQ/dx along the trajectory. In the next subsection, we show the performance of the overall track trajectory and dQ/dx fitting results with a few representative data events from MicroBooNE.

C. Performance

For most of the “good topology” tracks, the trajectory and dQ/dx fitting procedures are robust and accurate due to the excellent tracking and calorimetry performance of the LArTPC detector. However, there are several difficult cases where extra care was taken to ensure the fitting quality:

- An isochronous track where the track is parallel to the wire planes. This leads to large ambiguities in

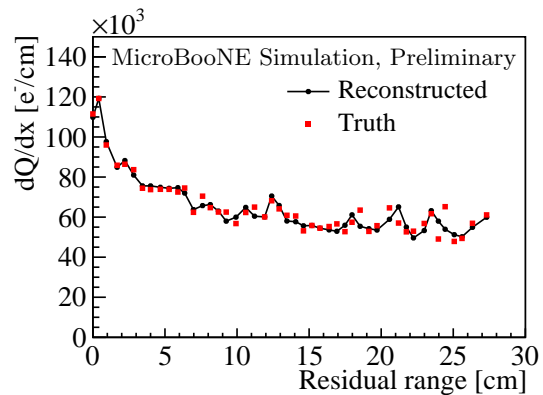


FIG. 4. The best-fit dQ/dx (in black) along a simulated muon track trajectory is compared with the true dQ/dx (in red) as a function of the residual range (track length counting from the stopping location).

determining the trajectory.

- A track that is compact from the collection (W) plane view. This leads to difficulty in assigning correct charges to the trajectory points.
- A track with parts of the segments in the non-functional channels, which leads to gaps in the track. This creates difficulty in both trajectory and dQ/dx determination, as they have to be inferred from the other wire plane views in the same time slice.

The key to dealing with these difficult cases is in the initial trajectory seed determination, which is described in detail in Appendix A. Figure 5 shows a typical “bad topology” track from MicroBooNE data. It touches the difficulties in all three categories. It is isochronous, compact in the W plane, and has gaps in the measurement due to non-functional channels in both U and W planes. Figure 5a shows the track topology from the side, end, and top views. The predicted light pattern (in green) is consistent with the measured light pattern (in red). Unresponsive area due to non-functional channels are shown in dark gray. Figure 5b shows the best-fit dQ/dx curve as a function of the track length. Since this track is a through-going muon (TGM), the dQ/dx fit is consistent with one minimum ionizing particle (1 MIP $\simeq 45k e^-/cm$) for most of the track segments. The high dQ/dx region corresponds to the segments with a delta-ray electron, and the dip near 100 cm is the result of an incorrect track trajectory fit near non-functional channels. Figure 5c shows the three projection views. The channels that have no measurement are non-functional. The magenta lines are the projection of the best-fit 3D trajectory in each wire plane view. The magenta circles correspond to the bad fit in dQ/dx around 100 cm. Despite this imperfection, the majority of the trajectory is

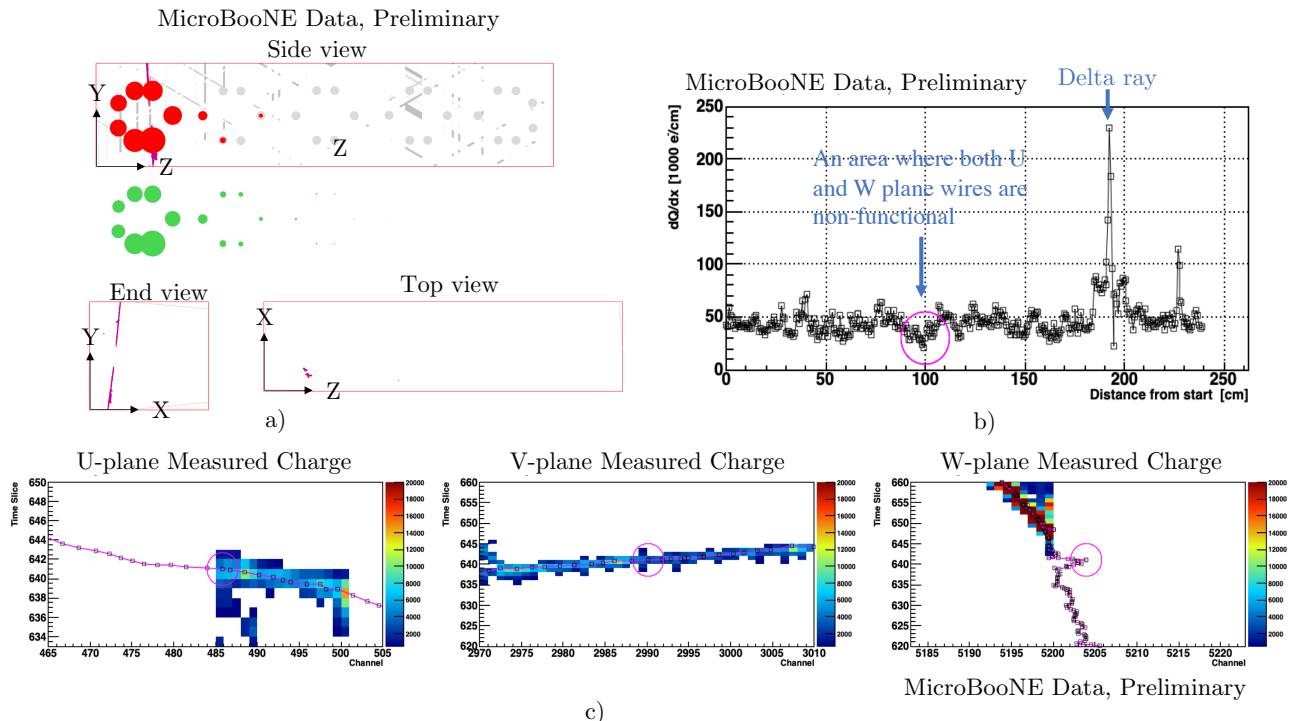


FIG. 5. Example of a typical “bad topology” track from MicroBooNE data. It is isochronous, compact in the W plane (see top view) where the “cross” shape comes from the cosmic-ray muon and its delta-rays. It has gaps due to non-functional channels in both U and W planes.

successfully determined, including a bridging of the gap corresponding to 100-170 cm in the best-fit dQ/dx curve.

As mentioned previously, accurate determination of dQ/dx is crucial in rejecting one of the main backgrounds to neutrino detection: the stopped muon (STM) background. Figure 6 shows such an example from a MicroBooNE data event. The side, end, and top views are shown in Figure 6a. The STM entered from the cathode side and stopped inside the detector. Figure 6b shows the best-fit dQ/dx curve as a function of the track length. The track is consistent with one MIP for most of the segments with a rise (Bragg peak) in dQ/dx at the end, which is a clear evidence of the muon stopping inside the detector. Further details on STM background rejection are described in Sec. V C.

The track trajectory and dQ/dx determination is important for achieving good particle identification (PID). Although not directly used in this work, we show such PID capabilities in Figure 7 with different simulated stopped charged particle tracks (Figure 7a) and a sample of ~ 2000 stopped muon tracks from MicroBooNE data (Figure 7b). The shape of the dQ/dx distributions from the STM data sample is consistent with those from simulated muons.

Figure 8 shows an example of a stopped proton from MicroBooNE data. The zoomed-in side, top, and end views are shown. Figure 8b shows the best-fit dQ/dx as a function of track length. While a typical MIP gives $45k e^-/cm$, this track gives about $100k e^-/cm$. A rise in

dQ/dx (Bragg peak) can be clearly seen. The shape of dQ/dx distribution is consistent with that from a simulated proton.

Figure 9 shows an example of one vs. two MIPs in a gamma pair production. Figure 9a shows the top and end views. One energetic delta ray (second MIP) is split from one MIP. At the beginning of the split, two MIPs are overlapping. Figure 9b shows the best-fit dQ/dx . When two MIPs are overlapped, $\sim 100k e^-/cm$ is obtained in dQ/dx , which is then reduced to $\sim 45k e^-/cm$ (1 MIP) after the two tracks become separate. This separation is crucial in achieving e/γ separation with a LArTPC.

V. REJECTING IN-BEAM COSMIC-RAY BACKGROUNDS

As described in Sec. III C, after the charge-light matching, the TPC cluster bundle that is matched to an in-beam flash is a neutrino interaction candidate. However, many of these candidates are actually cosmic-ray backgrounds that are in random time-coincidence with the in-beam flash. This is one of the major challenges for an on-surface LArTPC detector, such as MicroBooNE. The track trajectory and dQ/dx tools described in the previous section allow for further identification and rejection of these backgrounds. Two main cosmic-ray backgrounds are TGMs and STMs, which are described in Sec. V B and Sec. V C, respectively. The identification of

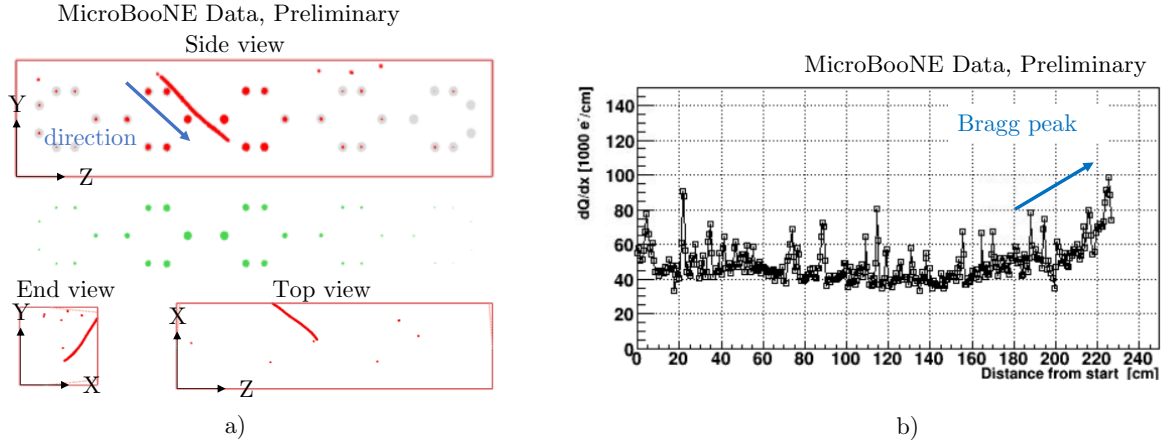


FIG. 6. Example of a stopped muon from MicroBooNE data.

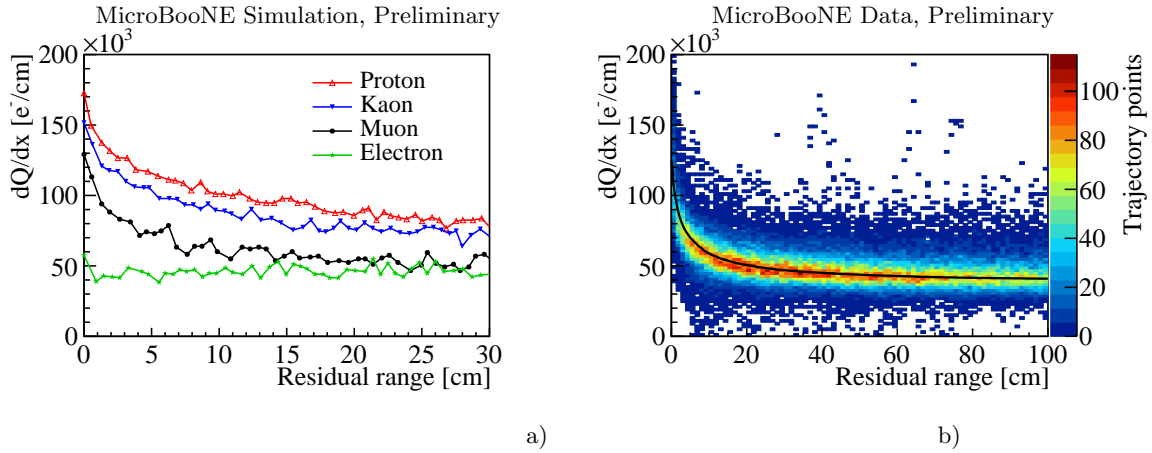


FIG. 7. (a) Examples of best-fit dQ/dx curves for different simulated stopped charged particles as a function of residual range (track length counting from the stopping location) using the fitting procedures described in this section. (b) The distribution of best-fit dQ/dx vs residual range from a sample of ~ 600 stopped muon tracks in MicroBooNE data. Color indicates number of trajectory points. The shape of the dQ/dx distribution are consistent with the model-predicted dQ/dx curve (black curve) of the muon. The model-predicted dQ/dx curve is scaled down by a factor here. More details of the model are described in Sec. V C.

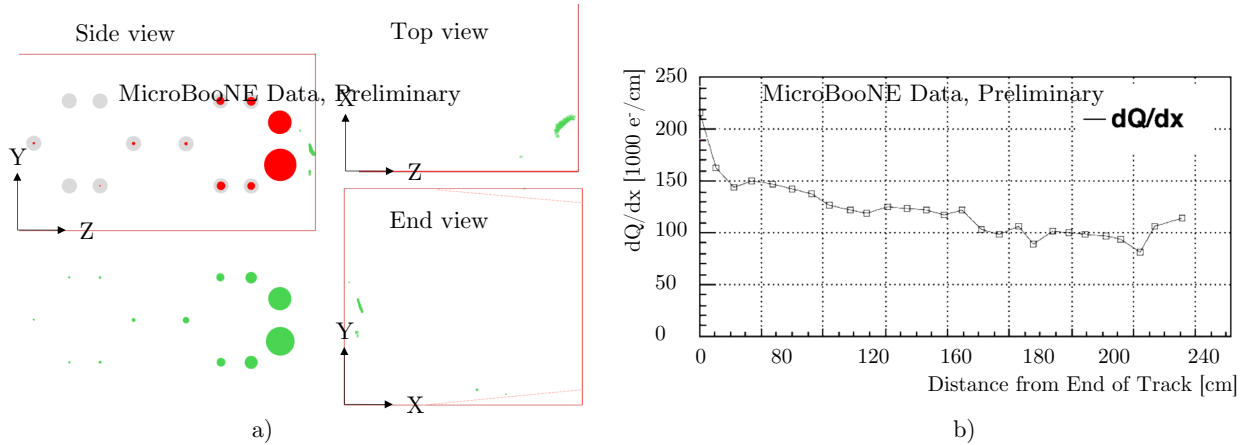


FIG. 8. Example of a stopped proton from MicroBooNE data.

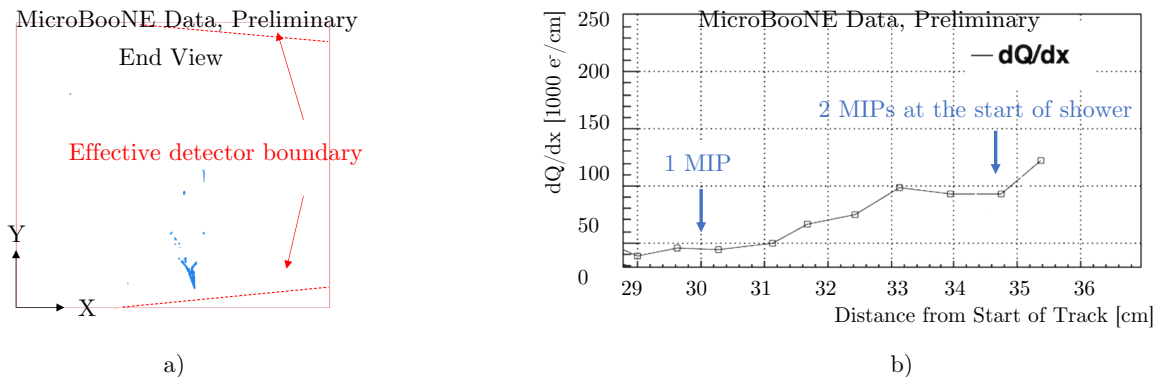


FIG. 9. Example of a gamma pair production.

these muons requires accurate knowledge of the effective detector boundary, which is introduced in Sec. V A. Finally, the charge-light matching results are re-examined in Sec. V D to remove certain light-mismatched candidates.

A. Effective boundary and fiducial volume

While the active TPC volume is a cuboid defined by the rectangular wire-planes at the anode and the corresponding cathode at the opposite end, the reconstructed TPC boundary from trajectories of charged particles, assuming that the ionization electrons drift along the externally applied uniform electric fields, deviate from the physical boundary because of the space charge effect. Understanding this effective TPC boundary is the key to identifying if a particle track is contained inside, entering, or exiting the detector.

The space charge effect [47, 48] comes from the fact that when ionization electrons drift toward the anode plane, the associated positively charged argon ions drift toward the cathode plane. Since the mass of the argon ion is much larger than the mass of the electron, the drift velocity of the ion is about five orders of magnitude slower. As a result, ions could take several minutes to travel a full drift distance. For on-surface LArTPC detectors like MicroBooNE, cosmic-ray muons provide a constant source of positively charged ions, leading to a large accumulation of positive charge inside the active volume and the distortion of the local electric field. As ionization electrons drift toward the anode plane, they are pulled by the positively charged ions toward the detector center. Consequently, the reconstructed position along the wire plane appears to be closer to the detector center compared to its true position, making the effective detector boundary smaller than the actual active TPC boundary. The more time the ionization electrons spend inside the active volume, the larger the position distortion is, which means that the deviation of the effective boundary from the physical boundary is larger for longer

drift distances. The detector boundary is mapped out from the observed distribution of entry and exit points of cosmic muons. To enhance the accuracy of this mapping, small, non-muon like clusters, and clusters at the beginning or end of the TPC readout winder, which are likely incompletely recorded, are removed.

A sample of about 1700 events from MicroBooNE data, each containing 20-30 cosmic muons, are used to map out the effective detector volume. The reconstructed 3D image points of the drift-time-corrected clusters are projected onto the X-Y (end view) and the X-Z (top view) planes. Figure 10 shows the zoomed-in views of the four corners at large drift distances, i.e near the cathode plane at ~ 256 cm in the X-direction, where the space charge effect is largest. The color represents the number of reconstructed points, where regions with little activity (blue) are outside the active TPC volume. The red lines represent the proposed effective detector boundary.

The projection of the effective detector boundary on the X-Y plane (end view) has a slight Z-dependence. This is studied by dividing the active TPC volume into 10 sub-volumes along the Z axis. The effective X-Y boundary of each sub-volume is calculated. The results for high Y and large X (top corner) are shown in Figure 11, and the Z-dependence is clear. Note that the proposed detector boundary in Figure 10 is conservatively estimated to be the inner boundary of all Z-slices. The effective boundary is also checked for different time periods during MicroBooNE data taking, and no clear time-dependence is observed.

A fiducial volume is further defined in the analysis for cosmic ray rejection and neutrino selection to mitigate the uncertainty in determining the effective boundary. The fiducial volume is defined as the inner volume at 3 cm away from all sides of the effective detector boundary. The total fiducial mass is 94.2% of the full 85 tons of liquid argon in the TPC active volume.

B. Through-going muons (TGM)

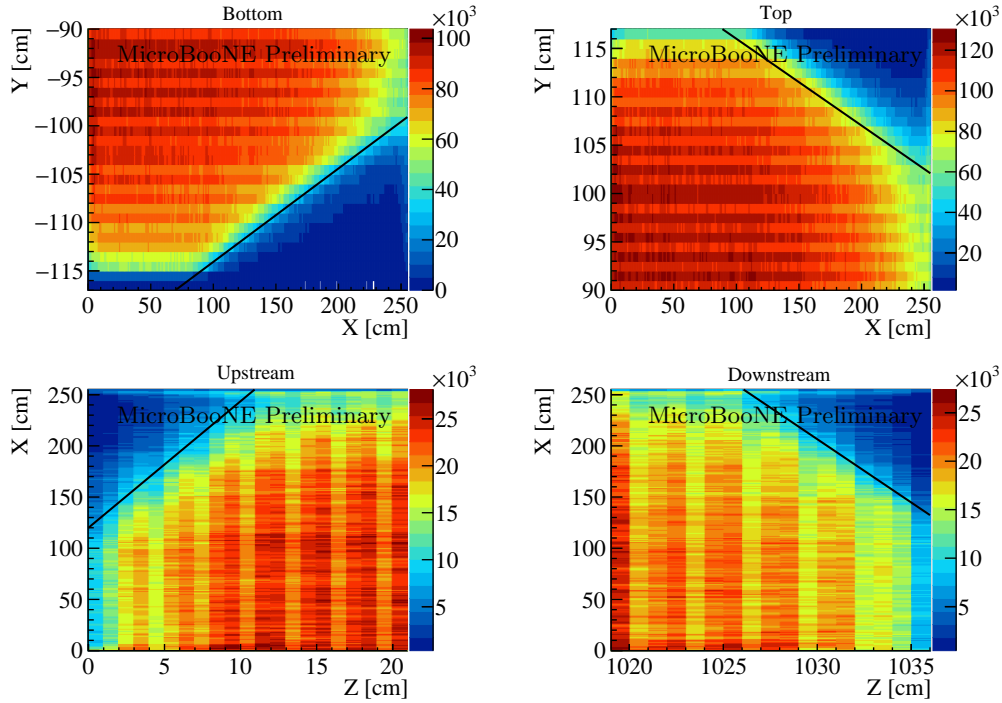


FIG. 10. The effective detector boundary (black lines) at the four corners of the detector. The color scale shows the map of cosmic-muon charge clusters in the detector.

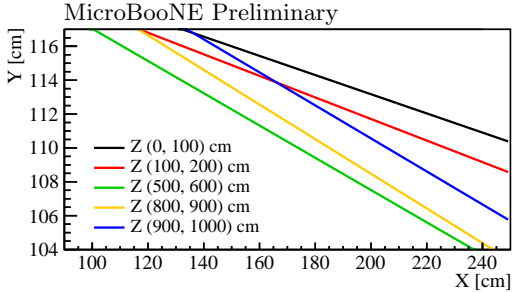


FIG. 11. Effective detector boundaries in the Y-X plane for the sub-volume at different Z-slices. A clear position dependence is shown.

The relatively slow drift velocity of the ionization electrons in the LArTPC results in a millisecond-level delayed TPC electronics readout. In general, there are 20–30 cosmic-ray backgrounds within each TPC readout window of 4.8 ms in MicroBooNE. After charge-light matching (Sec. III C), the activities inside the beam window are still dominated by cosmic-ray muons, with a neutrino signal to cosmic-ray background ratio of 1:6.4 (Table. I). Most of the cosmic-ray muons go all the way through the active TPC volume; therefore they are named through-going muons.

It is straightforward to identify a TGM with the effective boundary and fiducial volume defined previously. First, a set of extreme points of the corresponding TPC

cluster are found, including:

- the highest and lowest points in all three directions: vertical (Y) direction, drift direction (X), and beam direction (Z).
- the highest and lowest points in the vertical direction along the principle axis, determined by the principle component analysis (PCA), of the cluster.

If two of the extreme points are outside the fiducial volume boundary, this cluster is identified as a TGM, and these two points are defined as the two end points of the TGM. As a by-product, a fully contained event is tagged if all extreme points are inside the fiducial volume.

Two cases need special care to improve the TGM tagging accuracy:

- Gaps in the cluster caused by either non-functional channels or inefficient signal processing, which could lead to misplacement of the extreme points. This issue is mitigated by re-examining test points along the principle axis of the cluster against the known locations of the non-functional channels, and against the deconvolved signals from the original wire plane measurements.
- A neutrino interaction cluster where there are two separate particle tracks exiting the fiducial volume boundary, mimicking a TGM. This issue is caused by the simplified assumption that each cluster is a

single track-like object. Although a full multiple-track fitting algorithm is not developed for this work, a simplified algorithm to detect any large angle deflection along the track trajectory of the cluster is applied to protect against this case.

Figure 12 shows a typical TGM from MicroBooNE data. It enters and exits through the distorted TPC effective boundary due to the space charge effect.

C. Stopped muons (STM)

After rejecting the through-going muons, the largest remaining background comes from STMs, which enter the fiducial volume from outside and stop inside. A stopped μ^- decays to a positron with a lifetime of about $2.2 \mu\text{s}$. Only about 25% of stopped μ^- decay to an electron, with the rest getting captured by argon nuclei, reducing their lifetime to $0.57 \mu\text{s}$. The event topology of an STM therefore contains either only one track from the muon, or sometimes an additional short track from the Michel electron (energy up to $\sim 50 \text{ MeV}$) attached to the end of the muon track. Figure 6 in Sec. IV showed an example STM event from MicroBooNE data, and the best-fit dQ/dx along its track trajectory. Since the tracks from a neutrino interaction travel outward, the main discrimination of STMs relies on the determination of the track direction, which is through the identification of the entering point and then searching for a rise in dQ/dx consistent with the Bragg peak at the end of the track trajectory.

The entering point identification for an STM is similar to that for a TGM as described in Sec. V B. It is checked whether the extreme points of the corresponding TPC cluster are outside the fiducial volume after considering the non-functional channels and the inefficiency of the signal processing. The first-stage STM tagging then requires a single distinct entering point to be identified.

The track trajectory and dQ/dx fits are then performed as described in Sec. IV for the candidate STM cluster. In order to correctly determine the stopping point of the STM, a search for a large angle change (i.e. a kink) along the trajectory is carried out to identify a possible Michel electron track. If a kink is found, trajectory points from the entering point to the kink are labeled as belonging to the STM, while the rest of the trajectory points are labeled as belonging to its associated Michel electron. The track trajectory and dQ/dx fits are then repeated to further improve the accuracy for these two tracks. Figure 13 shows an example of an STM with a Michel electron attached to the end.

With the entering and stopping points, the track trajectory, and the dQ/dx determined, the final stage of STM tagging is based on a comparison of the measured dQ/dx with the predicted mean dQ/dx along its trajectory. For the prediction, the mean dE/dx of an STM is calculated from the PSTAR database [49], and

is checked for consistency with the Geant4 simulation. The modified-box model [50], which takes into account the recombination effect of ionization electrons, is used to convert the dE/dx to dQ/dx . The parameters of the model are taken from Ref. [51] and the calibration of the electronic response is taken from Ref. [36]. A residual discrepancy between the predicted dQ/dx and data was observed and it likely comes from the imperfect recombination model. In order to mitigate the impact from uncertain overall normalization of the reconstructed dQ/dx , Kolmogorov–Smirnov (KS) tests are utilized to determine the rise in a dQ/dx distribution.

For each STM candidate track, two KS tests are performed for the residual 35 cm of the track trajectory counting backward from the stopping point to check the consistency between the measured dQ/dx distribution and the references. The first KS test, KS_1 , is between the measured dQ/dx and the predicted dQ/dx of an STM. The second KS test, KS_2 , is between the measured dQ/dx and a MIP hypothesis using a flat dQ/dx prediction ($45\text{k e}^-/\text{cm}$). The two KS scores are then used to build an empirical discriminator: $\alpha = KS_1 - KS_2 + (|R_1 - 1| - |R_2 - 1|)/5$, where R_1 and R_2 are the two ratios between the prediction and the measurement of the integrated dQ/dx . The candidate track is identified as an STM if $\alpha < 0$. In addition, if there is a residual Michel electron track identified after the main STM track, the residual dQ/dx distribution and its track's (lack of) straightness are required to be consistent with the Michel electron hypothesis.

Several further checks are performed to increase the accuracy of the STM tagging: 1) Check for potential energetic delta rays on the trajectory path, which could impact the STM trajectory determination; 2) Take into account the cases where dQ/dx does not rise to its highest possible values when the muon decays in flight; and 3) Protect against a neutrino interaction being misidentified as an STM, similar to the cases in the TGM tagging. Figure 7 showed the measured dQ/dx distribution from a sample of ~ 2000 STMs identified in this work from MicroBooNE data. In Appendix B, we show several representative STM examples with difficult topologies or unusual dQ/dx distributions.

D. Light-mismatched (LM) events

The third largest in-beam background, next to the TGM and STM backgrounds, comes from light-mismatched (LM) events, where the observed light pattern on the PMTs does not agree with the prediction from the matched TPC clusters. This could happen because the charge-light matching procedure as described in Sec. III C intends to be more inclusive when matching clusters, with an expectation that later reexamination is necessary to improve the matching accuracy.

The majority of the LM events contain only small clusters that give very low-intensity predicted light. The typ-

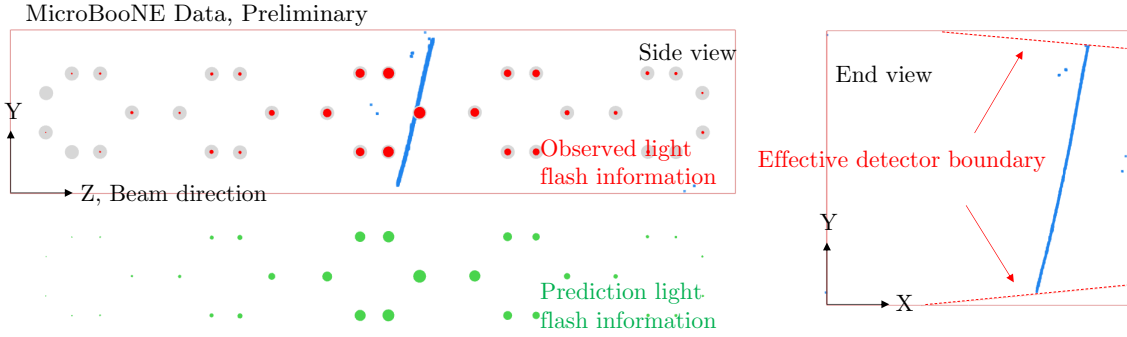


FIG. 12. Example of a TGM entering and exiting through the distorted TPC effective boundary due to the space charge effect. The red (green) circles represent the observed (predicted) light flash information. The consistency between them indicates correct charge-light matching.

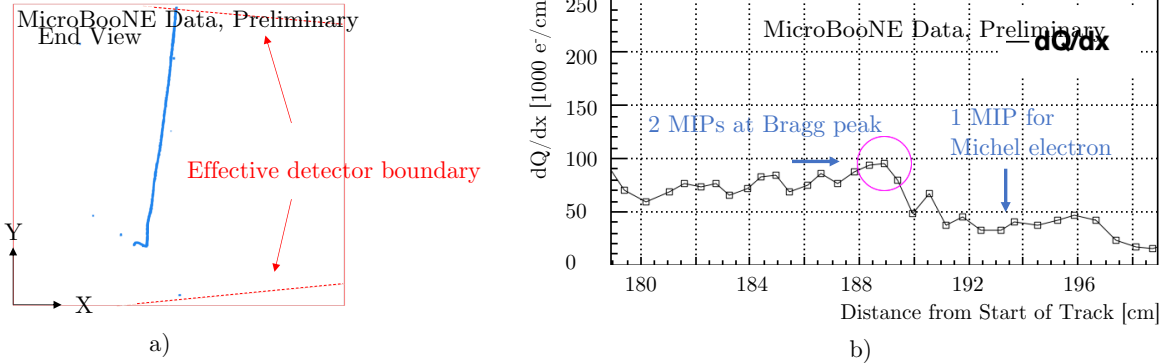


FIG. 13. An STM candidate with a short stopped muon track following by a Michel electron.

ical energies of these clusters are a few MeVs, and it is challenging to correctly match those low energy dot-like activities to their predicted light patterns. The length of the cluster and the intensity of the predicted and measured light are used to tag and remove those low-energy events.

A Kolmogorov–Smirnov (KS) test is then performed between the observed and the predicted light pattern without the normalization constraint to tag candidate LM events with higher energy. They are usually caused by the inefficiency of the PMT system to detect cathode-side events, the light production outside of the TPC active volume, or the inaccuracy of the photon library for anode-side events. If the KS test score is extremely low, the cluster is directly tagged as an LM event and rejected. If the KS test score indicates a modest inconsistency, a further check is performed to see if the LM candidate can match a different light flash from the cosmic discriminator, and if it is consistent with either a through-going muon or a stopped muon. This check relies on the precise knowledge of the effective boundary that is distorted by the space charge effect, and so the Z-dependent effective boundary as shown in Fig. 11 is used. Firstly, any such candidate LM cluster is paired with the other

flashes in the PMT readout window. Under the new pair of flash-cluster hypotheses, the LM cluster is placed at a different drift location given the new flash time. Several scenarios follow:

- If a new flash is found to be more consistent with the cluster prediction, and the cluster has two end points on the effective detector boundary, this cluster is then re-tagged as a TGM and rejected.
- If a new flash is found to be more consistent with the cluster prediction, and the cluster has only the entering point on the effective detector boundary, this cluster is tagged as a possible STM and then vetted by the STM tagger (Sec. VC) to confirm and reject.
- If no new flashes are more consistent with the cluster prediction, but the cluster can be moved along the drift direction such that both end points exactly touch the effective boundary, this cluster is also re-tagged as a TGM and rejected. The associated flash is assumed to be lost in the light detection or flash reconstruction (Sec. III A). The boundary contact tolerance is made more stringent in order

for the TGM to be determined purely by the geometric information.

The TGM, STM, and LM background taggers are applied in order after the charge-light matching step to remove most of the in-beam backgrounds. The remaining events are the neutrino candidates. In the next section, we evaluate the performance of this generic neutrino detection procedure.

VI. PERFORMANCE OF THE GENERIC NEUTRINO DETECTION

In this section, we evaluate the performance of the generic neutrino detection, i.e. cosmic-ray background rejection, in terms of the neutrino selection efficiency, purity, and cosmic ray rejection power. Three samples are used for this evaluation:

- *BNB*: a partial dataset of an on-beam “open” data sample recorded from February to April 2016, triggered by BNB neutrino spills (30k events after software trigger).
- *EXT*: a partial dataset of an off-beam data sample taken during the periods when no beam was received, recorded from February to April 2016, pure cosmic background (30k events after software trigger).
- *MC*: simulated neutrino interactions from BNB overlaid with an EXT data sample. Each MC event has one simulated neutrino interaction uniformly distributed in the liquid argon volume inside the TPC cryostat, of which 44% is the TPC active volume (540k events). A special MC “dirt” sample is also used where each event has one simulated neutrino interaction outside the cryostat liquid argon volume, as far as about 20 meters into the experimental hall (90k events). Official MicroBooNE cross section modeling (tuned GENIE v3) was used in the simulation.

A series of cuts are applied in sequence to select neutrino interactions and reject cosmic-ray backgrounds from the original hardware triggers initiated by beam spills: 1) offline light filter; 2) charge-light matching; 3) TGM rejection; 4) STM rejection; and 5) LM event rejection. The techniques implemented in each cut were described in previous sections. The neutrino selection efficiency for ν_μ CC and ν_μ NC events, the cosmic-ray reduction factor, and the neutrino signal to the cosmic-ray background ratio for each cut are evaluated from the MC and EXT samples, and summarized in Table I. In practice, the software trigger is applied before the offline light filter for a first-stage data reduction. However, since the software trigger requirement is a subset of the offline light filter algorithms in this work, the two cuts are combined together in the table. The efficiency

for each channel is calculated for events generated in the fiducial volume only. The fiducial volume requirement itself has an efficiency of 94.2%, and is counted separately. The overall selection efficiency of the neutrino interactions in the fiducial volume, integrated over the entire energy range of the BNB spectrum, is 80.4% for ν_μ CC interactions and 35.9% for ν_μ NC interactions, respectively. The cosmic-ray reduction factor is calculated by counting individual cosmic-ray tracks in the TPC readout window before and after each cut. An overall cosmic-ray rejection power of $\sim 1.5 \times 10^5$ is achieved, resulting in a neutrino signal to cosmic-ray background ratio of 5.2 to 1. In the final selected events, there are additional 10% neutrino interactions which originate outside the fiducial volume and are not taken into account in this ratio.

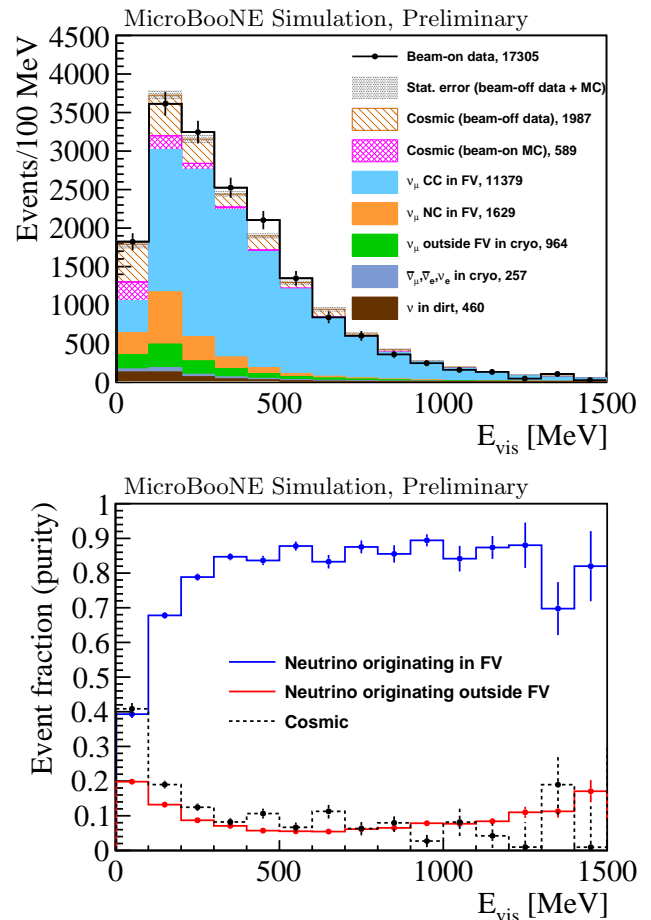


FIG. 14. (Top) The stacked MC and EXT events are compared with the final selected events from the BNB sample. Selected events are further categorized based on MC truth. All numbers are scaled to 5×10^{19} POT. (Bottom) Event fraction, i.e. purity, of the selected events. See text for more discussions.

The final selected events including all categories are shown in Figure 14. In the top panel, the selected MC and EXT events are stacked to compare with the BNB events as a function of the calibrated visible energy [51],

TABLE I. Summary of the cumulative neutrino selection efficiency, over all energies, for ν_μ CC and ν_μ NC events in the fiducial volume (94.2% of the active volume), the cosmic-ray reduction factor, and the neutrino signal to the cosmic-ray background ratio for each cut. The relative cosmic-ray reduction to the previous cut is shown in the parentheses. The last column shows the generic neutrino signal to cosmic-ray background ratio. Neutrinos originating outside the fiducial volume are not counted in this table. See Figure 14 for more details of the selected neutrino candidates.

Cut	ν_μ CC efficiency	ν_μ NC efficiency	Cosmic-ray reduction	ν : cosmic-ray
Hardware trigger	100%	100%	1 (1)	1 : 20k
Offline light filter	98.3%	85.4%	0.01 (0.01)	1 : 210
Charge-light matching	92.1%	53.6%	2.6×10^{-4} (0.026)	1 : 6.4
TGM rejection	88.9%	52.1%	4.4×10^{-5} (0.17)	1.1 : 1
STM rejection	82.9%	50.3%	1.4×10^{-5} (0.32)	2.8 : 1
LM rejection	80.4%	35.9%	6.9×10^{-6} (0.50)	5.2 : 1

E_{vis} , which is converted from the total charge measured by the collection wire plane, taking into account the recombination and attenuation of the ionization electrons. All reported numbers are scaled to an integrated neutrino beam intensity of 5×10^{19} protons on target (POT). The cosmic-ray background is estimated from the EXT beam-off data sample. An additional cosmic-ray background only when beam is on is estimated from the MC sample, which corresponds to a cosmic-ray cluster being incorrectly matched to the neutrino-induced flash but passing the LM cut. Neutrino events are categorized based on their interaction type: charged current (CC) or neutral current (NC), and their location: inside fiducial volume (FV), inside the liquid argon volume (cryo), or outside the liquid argon volume (dirt). The error bars for the data and MC samples are statistical only. The event fraction, i.e. purity, of the selected events is shown in the bottom panel as a function of the visible energy. About 10% of selected events are from neutrinos originating outside the fiducial volume. They are not counted in the efficiency calculation in Table I. For generic neutrino detection, if only cosmic-ray backgrounds are considered as impurity, an overall 85.1% purity is achieved, and for visible energy greater than 200 MeV it is 90.3%.

Figure 15 shows the cumulative selection efficiencies after each cut as a function of the visible energy. The efficiency calculation is performed for ν_μ CC and ν_μ NC interactions in the fiducial volume separately. The overall efficiency for ν_μ CC events is 80.4%, where 88.4% is achieved for visible energy greater than 200 MeV. The overall efficiency for ν_μ NC events is 35.9% because of their typically low energy depositions that enhance the contributions from the low-energy bins (<100 MeV). The conversion between the calibrated visible energy (E_{vis}) and the deposited energy (E_{dep}) from MC truth is shown in Figure 16. The efficiency drop in the E_{vis} region of 500-1000 MeV for NC events as shown in the bottom panel of Figure 15 corresponds to an inefficient separation of cosmic activity and NC interaction final state particles in the charge-light matching. Though the selection of low E_{dep} NC events is most likely to fail in the matching stage, some of them could be clustered with cosmic activity and collectively matched to the in-beam

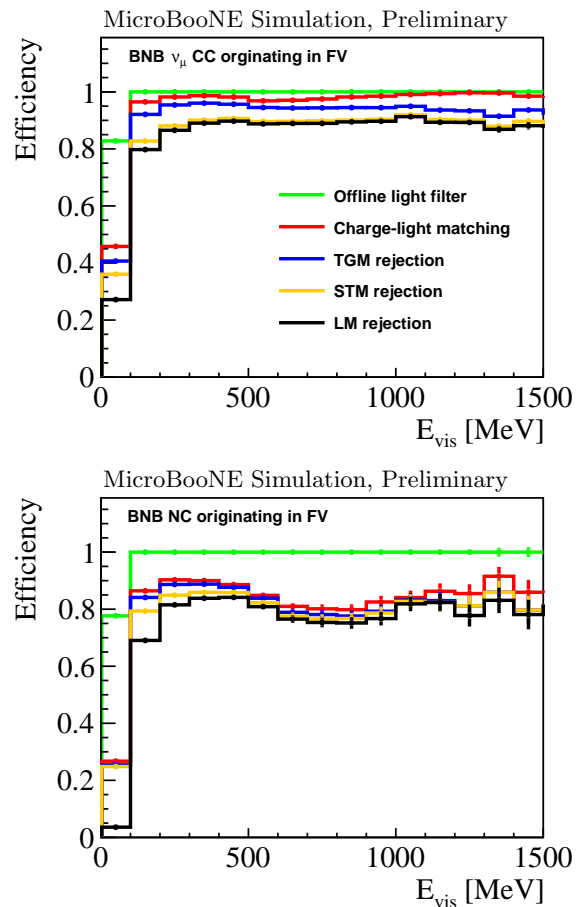


FIG. 15. Efficiency of the neutrino interactions originating in the fiducial volume as a function of the visible energy. (Top) Efficiency for BNB ν_μ CC interactions. (Bottom) Efficiency for BNB ν_μ NC interactions. The efficiency drop in the 500–1000 MeV region corresponds to improper charge-light matching for some low E_{dep} NC events.

PMT signals. This results in a much greater value of E_{vis} than E_{dep} as shown in the bottom panel of Fig. 16. These events are the origin of the efficiency drop as mentioned above. Further improvements on the removal of residual cosmic activity and visible energy calibration are

expected in the downstream pattern recognition and neutrino energy reconstruction.

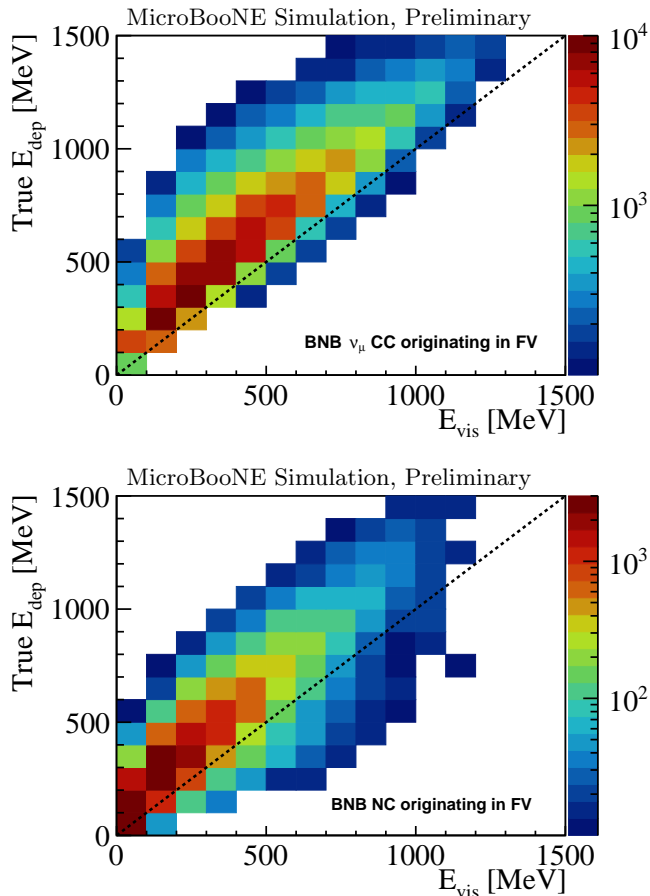


FIG. 16. Comparison of the true deposited energy (E_{dep}) and the calibrated visible energy (E_{vis}). (Top) For BNB ν_{μ} CC interactions. (Bottom) For BNB ν_{μ} NC interactions.

The generic neutrino detection procedures described in this paper mark the beginning of a high-performance selection of individual neutrino interaction channels, which requires additional particle-level pattern recognition and reconstruction techniques. Several algorithms were developed in MicroBooNE and applied in previous publications, such as Pandora [52], Deep Learning [53, 54], Multiple Coulomb Scattering [43], electromagnetic shower reconstruction [55], etc. More pattern recognition tools are in development including those within the Wire-Cell reconstruction. Nevertheless, it is interesting to compare the performance of the cosmic rejection and generic neutrino selection in this work with those from previous results in Refs. [16, 26–28]. The cosmic rejection in this work is enhanced by a factor of 8 compared to the cosmic rejection power (without kinematical requirements) published in Ref. [27]. The number of selected ν_{μ} CC events for 5×10^{19} POT is about 4.3k in Ref. [28], with an overall cosmic contamination of 35.5% in the final selection. In comparison, the number of selected ν_{μ} CC

events is expected to be 11.3k with this generic neutrino detection procedure, with an overall cosmic contamination of 14.9% in all neutrino candidates. The increase in number of events comes from both the enhancement in the selection efficiency and the enlargement of the fiducial volume.

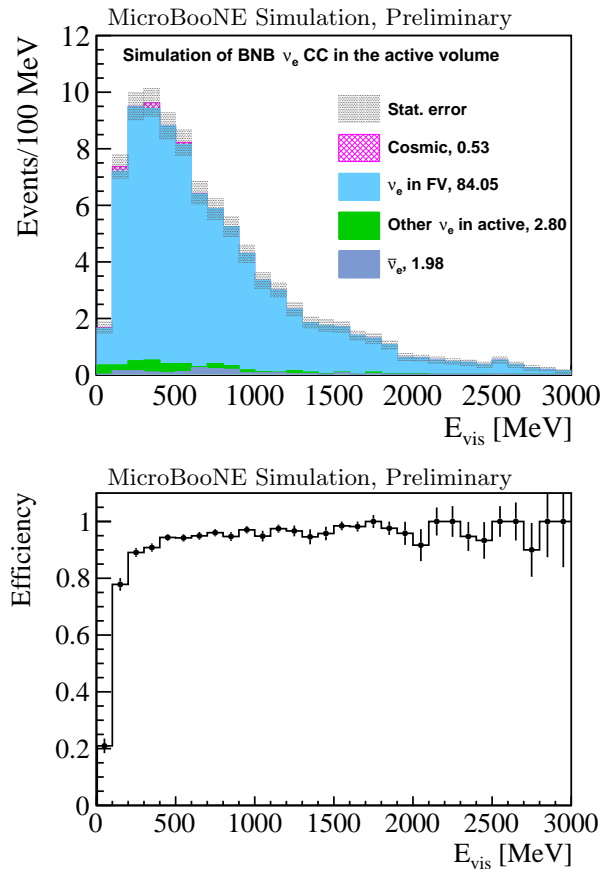


FIG. 17. (Top) Composition of the selected events from the BNB ν_e CC sample after scaling to 5×10^{19} POT. Only ν_e CC interactions are simulated in the TPC active volume. (Bottom) Efficiency for ν_e CC interactions originating in the fiducial volume as a function of the visible energy.

Finally, a special MC sample with only ν_e CC interactions from the BNB intrinsic ν_e flux, overlaid with EXT data, is used to estimate ν_e CC efficiency under this selection procedure. The expected number of the ν_e CC events in the TPC active (fiducial) volume for 5×10^{19} POT is 100 (95) in total. Figure 17 shows the composition of the selected events and the selection efficiency as a function of the visible energy. The overall ν_e CC event selection efficiency is 87.6%. This high efficiency for ν_e CC events is particularly important for future MicroBooNE analysis to investigate the nature of the low-energy excess of ν_e -like events observed in the MiniBooNE experiment [14]. The remaining challenge of improving the ν_e CC selection purity is still an active research area.

VII. SUMMARY AND OUTLOOK

This paper describes various novel techniques developed in the Wire-Cell event reconstruction paradigm to achieve a high-performance generic neutrino detection in MicroBooNE. In particular, a high rejection factor of the cosmic-ray background is achieved for the first time for a large LArTPC detector running on the surface, while keeping the neutrino detection efficiency high. The significant improvement in performance compared to previous published results provides a solid foundation for the upcoming physics analyses in MicroBooNE and marks a major milestone in demonstrating the full capability of LArTPCs in neutrino physics. Further development of particle-level pattern recognition and reconstruction techniques toward selections of individual neutrino interaction channels are in progress in Wire-Cell, and will be reported in future publications.

ACKNOWLEDGMENTS

This document was prepared by the MicroBooNE collaboration using the resources of the Fermi National Accelerator Laboratory (Fermilab), a U.S. Department of Energy, Office of Science, HEP User Facility. Fermilab is managed by Fermi Research Alliance, LLC (FRA), acting under Contract No. DE-AC02-07CH11359. MicroBooNE is supported by the following: the U.S. Department of Energy, Office of Science, Offices of High Energy Physics and Nuclear Physics; the U.S. National Science Foundation; the Swiss National Science Foundation; the Science and Technology Facilities Council (STFC), part of the United Kingdom Research and Innovation; and The Royal Society (United Kingdom). Additional support for the laser calibration system and cosmic ray tagger was provided by the Albert Einstein Center for Fundamental Physics, Bern, Switzerland.

Appendix A: Trajectory seed finding

As described in Sec. IV A, both the 2D images from wire plane measurements after signal processing (Sec. III B 1) and the Wire-Cell 3D imaging results (Sec. III B 2) are used in the track trajectory and dQ/dx fitting. Graph theory plays an important role in constructing an initial seed of the 3D trajectory, which is essential for associating the nearby 2D pixels for the trajectory fit. The quality of the initial seed finding impacts the quality of the final fit.

Figure 18 shows two examples illustrating the importance and challenges of constructing the 3D trajectory seed. When a track is traveling close to parallel to the wire planes (also referred to as an isochronous topology), the associations among wires from different planes at the same time slice are no longer obvious. This ambiguity

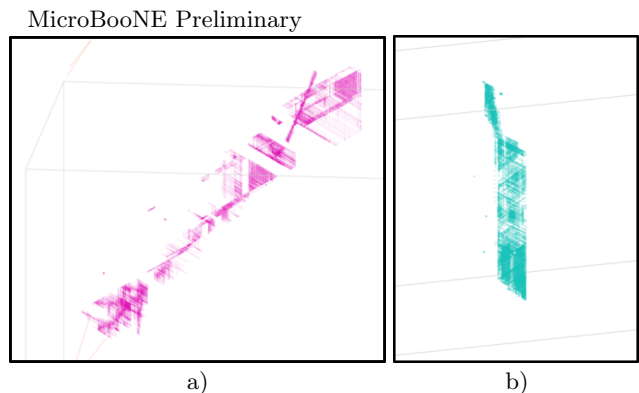


FIG. 18. (Left) An example of an isochronous track with gaps. Some of the gaps are results of non-functional channels, while others are results of the coherent noise removal during the excess noise filtering step [33]. (Right) An example of an isochronous track that is also compact with respect to the vertical W collection wires.

typically leads to mistakes in forming associations, which further propagate to the trajectory and dQ/dx fits. In addition, gaps can occur in the reconstructed 3D images (Fig. 18a), which have two typical origins. First, gaps can be the results of the $\sim 10\%$ non-functional channels [33], which are spread across different views. Second, gaps can be created when small coherent signals (e.g. when a track travels parallel to the wire plane) are accidentally removed by the coherent noise removal [33] or by the TPC signal processing procedure [35, 36]. For induction wire planes, the current TPC signal processing procedure shows inefficiency for extended signals in time, which is referred to as the *prolonged* track topology. For this topology, the raw signal is typically small, leading to difficulties in constructing the signal region of interest. The algorithm constructing the track seeds takes into account these imperfections through using advanced graph theory operations. The central idea is to find the shortest path between points of interest on a Steiner-tree inspired graph, the construction of which takes into account the additional charge information. In the following, we describe the details of the related algorithms.

Overclustering protection: The result of the charge-light matching described in Sec. III C is a matched bundle which consists of 1) a PMT flash, 2) the main TPC cluster, and 3) secondary clusters. As described in Sec. III B 3, the separation of different clusters is largely based on connectivity and proximity, with dedicated algorithms to mitigate gaps. The main cluster is defined to be the cluster which provides the largest contribution to the observed PMT flash. The track trajectory and dQ/dx fits are thus performed only on the main cluster.

Since the clustering algorithm mainly focuses on the separation of different interactions, there is a small number of events in which the main cluster has a problem of overclustering, that is, the grouping of separated clusters into a single cluster. One common cause of the overclus-

MicroBooNE Preliminary

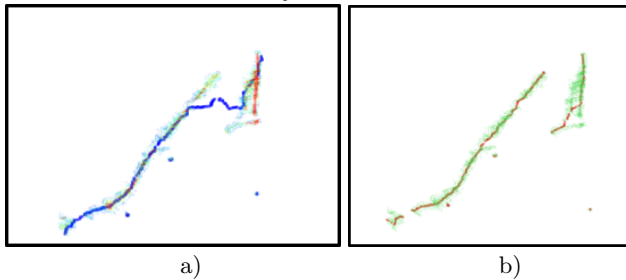


FIG. 19. (Left) Track seed before applying the overclustering protection. A track seed (blue points) is constructed going through two separated clusters. Space points are displayed with their average charge information as colors. Red and blue colors represent high and low charge, respectively. (Right) Track seed after applying the overclustering protection. Two clusters (red points) are separated. Space points are displayed as green points without charge information.

tering is from incorrect gap mitigation. A re-examination of the matched bundle is performed to protect against overclustering. First, all blobs from the matched clusters are collected as the input to a new clustering algorithm. Each blob is treated as a vertex in a graph. Second, edges are established between blobs that are evidently connected. For example, if two blobs in adjacent time slices are overlapping in the transverse direction (parallel to the wire planes), they are defined to be connected. Third, additional edges are established to mitigate gaps. This algorithm improves upon the original clustering algorithm (Sec. III B 3) with slightly different criteria. Finally, the new cluster with the most overlap with the original main cluster is set as the new main cluster for the matched bundle. Figure 19 shows the improvements after implementing the overclustering protection algorithm.

Overcoming gaps: As described previously, despite the LArTPC being a fully active detector, gaps can occur in a charged particle track due to various hardware or software issues. The gaps present a serious challenge to the trajectory fitting, and a retiling algorithm is introduced to overcome this problem. Figure 20 shows the performance of two rounds of the retiling step. During the first round, the known non-functional channels are assumed to be live during the tiling step of the 3D image reconstruction (Sec. III B 2). Since the 3D image reconstruction is limited within the current cluster instead of the entire event, this procedure does not create many spurious blobs. The middle figure of Fig. 20 shows the reconstructed 3D image after filling the known non-functional channels. Improvement in terms of removing gaps is obvious. The remaining gaps are the result of the inefficient channels, where signals are lost as the result of either the coherent noise removal or signal processing. A second round of retiling is performed to deal with inefficient channels. First, the highest and lowest space points in the vertical direction are found in the current cluster. On the associated graph, a Dijkstra’s shortest path algo-

rithm [56] is used to find the shortest path between these two 3D points. The path can go through gaps in the image, although it may not locate at the correct place on the 3D image. Despite this issue, the shortest path is projected to each of the three 2D time-versus-wire views. 2D pixels close to the projected path are treated to be live independent of their original states. This effectively fills the inefficient channels and a new round of tiling is performed. The right column of Fig. 20 shows the reconstructed 3D image after the second round of retiling. Gaps from the inefficient channels are successfully filled.

Steiner-tree inspired graph construction: Naively, the 3D trajectory seed can be obtained by finding the shortest path on the constructed graph after two rounds of retiling in the previous step. However, the resulting seed sometimes significantly deviates from the true trajectory. The situation can be improved by implementing a Steiner-tree inspired graph, which can force the seed to go through important points in the graph. In mathematics, given an undirected graph with non-negative edge weights and a subset of selected vertices (terminals), the Steiner-tree problem is to find the tree with minimum total weights (the minimal spanning tree) that contains all selected terminals. Mapping to our problem, the Steiner-tree terminals are selected to be the 3D points (also vertices in the graph) that are associated with high charges in the three views. The Steiner tree would then be guaranteed to go through these high-charge points, which are more likely to be close to the true track trajectory. Figure 21a shows that the selected Steiner terminals are along the middle of the available 3D space points. Figure 21b shows both the selected terminals and non-terminals in a Steiner tree.

Mathematically, the Steiner-tree problem is an NP-complete (non-deterministic polynomial-time complete) problem. Therefore, the actual implementation is through an approximated solution considering the cost of the computation. The Steiner Tree Greedy Algorithm in the Practical Approximation Algorithm [57] is used. In this algorithm, the Voronoi regions around the selected terminals are constructed (In mathematics, a Voronoi diagram is a partition of a plane into regions close to each of a given set of objects.) The shortest path between any two adjacent terminals with their Voronoi regions connected is constructed. The Steiner tree then becomes the minimal spanning tree of the newly constructed graph, which we call the Steiner-tree inspired graph. Figure 22 shows an example of the shortest path on a Steiner-tree inspired graph, which is used in this work as the initial trajectory seed. In the following, we describe in more details how the Steiner-tree inspired graph is constructed.

A first-stage graph for a cluster is constructed as follows: First, the cluster goes through two rounds of retiling to mitigate gaps. Second, each of the three 2D projection views of a blob is examined. The two views with the longest and shortest channel extensions are found. 3D points are created at the crossing of wires from these two views with certain spacing, which reduces the amount of

MicroBooNE Preliminary

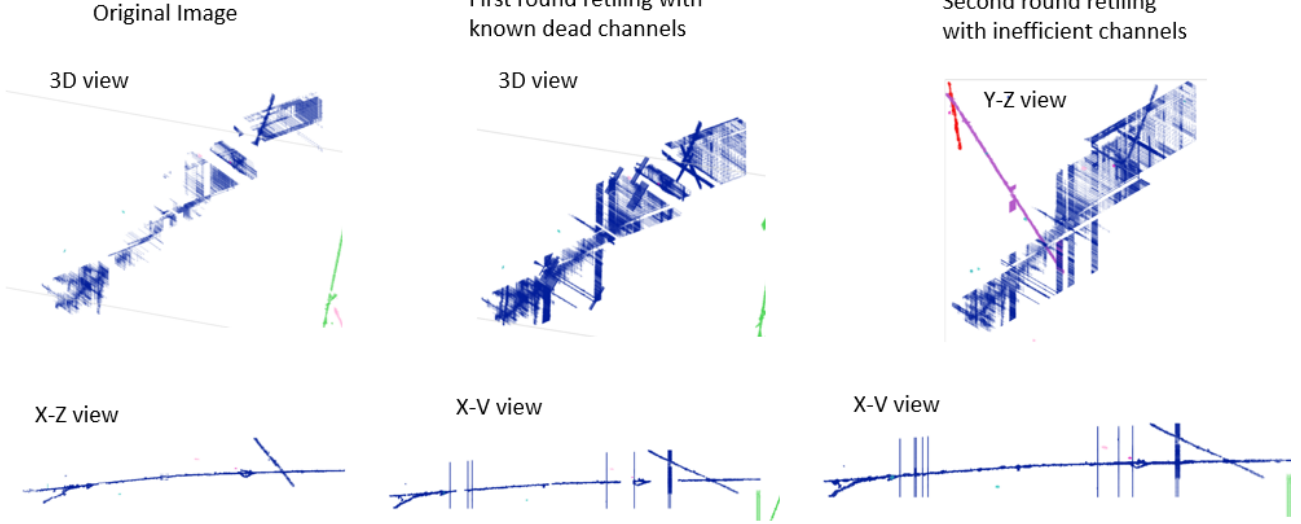


FIG. 20. Illustration of the retiling step. (Left) Original images are shown for 3D (top) and X-Z projection (bottom) views. (Middle) The same images after the first round of retiling when the known non-functional channels are filled. (Right) Same images after the second round of retiling where the inefficient channels are filled.

MicroBooNE Preliminary

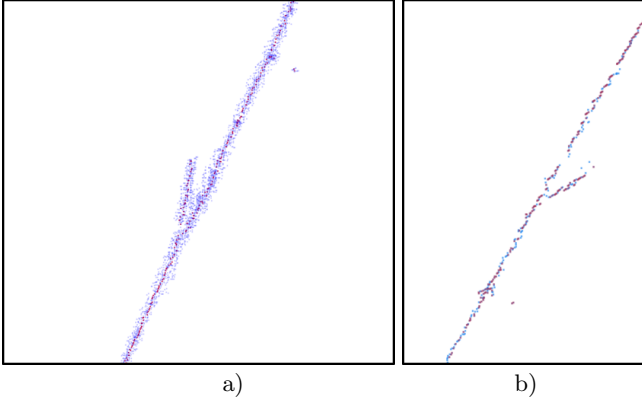


FIG. 21. In both views Steiner terminals are shown in red. On the left, all 3D space points are shown in blue, while on the right only those selected by the Steiner tree are shown.

computer memory usage. Additional space points where the charge on wires is larger than a certain threshold (4000 electrons as a default) are added. The creation of latter points also considers the third view, which guarantees that all points with high charges are properly included. Third, a graph is created with these 3D points as vertices. Edges between vertices in the same blob are established when their distance is smaller than a predefined value. The weight of the edge is assigned as the distance between the two points. Edges connecting points from different blobs within two adjacent times are created under the same predefined distance threshold. Finally, the connected components algorithm [58] is used to find the disconnected sub-graphs. Additional edges are estab-

MicroBooNE Preliminary

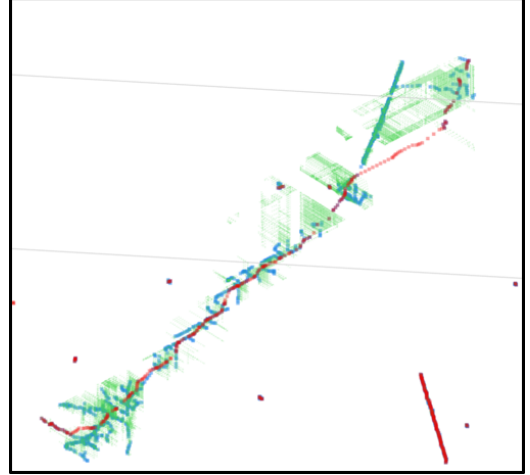


FIG. 22. An example of the shortest path on the Steiner-tree inspired graph (red points). Green points represent original space points. Blue points are the selected Steiner terminals.

lished between these disconnected sub-graphs according to the distance and directional information: First, between any two sub-graphs, the pair of points with the closest pair of points is found. The direction is then calculated by performing a Hough transformation inside a sub-graph with the selected point as the origin. If the directions of both sub-graphs are aligned, an edge is created.

The Steiner-tree inspired graph is then constructed. First, Steiner-tree terminals are found inside the first-stage graph. For each vertex (3D point), the three cor-

MicroBooNE Preliminary

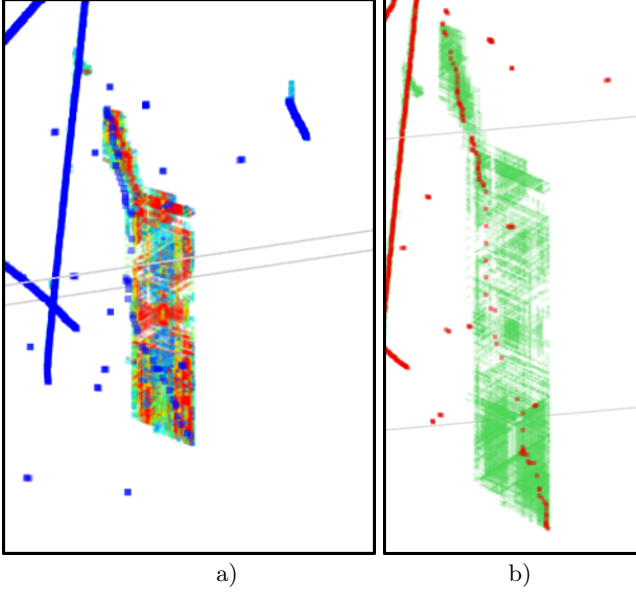


FIG. 23. Impact of the same-blob Steiner edges. (Left) The shortest path (blue points) without adding the same-blob Steiner edges is along the boundary of the 3D image. This is partially caused by the grid structure of space points. Space points are displayed in colors with charge information. (Right) The shortest path after adding the same-blob Steiner edges (red points). Space points are displayed as green without the charge information.

MicroBooNE Preliminary

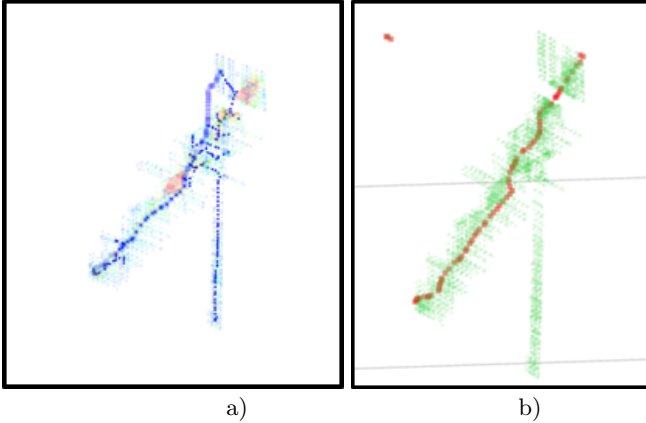


FIG. 24. Improvement in searching for end points. (Left) Extreme points identification based on the principle component analysis. Space points are displayed in color with charge information. The shortest path is shown as blue points. (Right) Current extreme points identification. Space points are displayed as green points without charge information. The shortest path is shown as red points.

responding 2D pixels (one on each view) are found. The charge of each vertex is calculated to be the average charge of the three 2D pixels. Any vertex with its average charge higher or equal than all its neighbors on the first-stage graph is defined as a Steiner-tree terminal.

MicroBooNE Preliminary

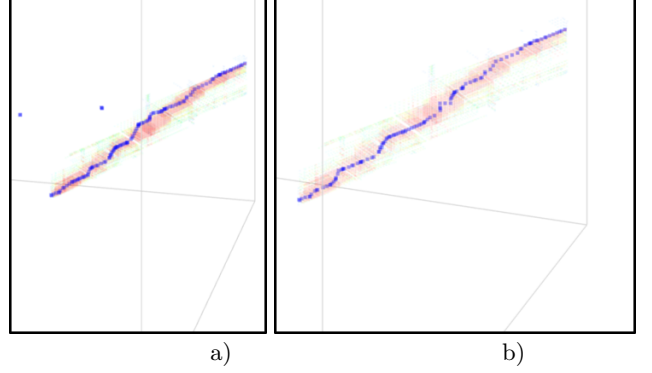


FIG. 25. Impact of adding charge information to the weight calculation. Blue points represent the shortest path. Space points are displayed in colors with their charge information. (Left) Weights are calculated only according to distances. (Right) Weights are calculated including the charge information.

A predefined threshold is applied to remove points with very low charge. Second, for each terminal, every other point inside the same *blob* is connected to it with an edge, which avoids the creation of grid points. Figure 23 shows the improvement in building the shortest path with these same-blob Steiner-tree edges. Third, two extreme space points of the first-stage graph, which are defined to cover the most live channels and time slices, are found. Figure 24 shows the comparison of the path construction using the old and new extreme-points searching algorithm. The original algorithm begins by finding the two points that have the largest separation along the main axis of the cluster. The shortest path between two extreme points is found using the Dijkstra shortest path algorithm. This path is essential for excluding spurious Steiner-tree terminals with isochronous track topologies. Terminals with their 3D distances to the aforementioned shortest path larger than a certain distance (6 cm as the default) and 2D distances in two projection views smaller than another distance (1.8 cm as default) are excluded. Finally, the Steiner-tree inspired graph is constructed. For edges constructed on the Steiner-tree inspired graph, a slightly different weight (w) is calculated, using the charge information as follows:

$$w = \Delta r \left(0.8 + 0.2 \times \left(\frac{Q_0}{Q_s + Q_0} + \frac{Q_0}{Q_0 + Q_t} \right) \right),$$

with $Q_0 = 10^4$ electrons, and Q_s and Q_t being the average charge of the starting and ending vertices, respectively. Δr represents the original distance between the two vertices. This choice leads to a slightly smaller weight for edges connecting two high-charge points. Figure 25 shows the impact of adding the charge information to the weight calculation. The shortest path is found on the Steiner-tree inspired graph. The initial trajectory seed for the track trajectory fitting is chosen from the the shortest path such that the distance between two ad-

jacent points is not too small nor too large (1 cm for the coarse-spacing fit and 0.6 cm for the fine-spacing fit, as described in Sec. IV). This operation leads to a more uniform set of seed points to produce the desired spacial granularity.

2D pixel association: During the track trajectory fit, the associations between the 3D points and 2D pixels need to be formed, so that only a limited number of 2D pixels participate in determining each track trajectory point. This association is aided by the initial trajectory seed. The 3D points (vertices) on the first-stage graph close to the initial trajectory seed are found, and their parent blobs are saved. These 3D blobs are projected to the three 2D views to find the close-by 2D pixels (within 90% of the projected 2D distance) to associate. This procedure is repeated on the Steiner-tree inspired graph, which helps to bridge the gaps in the original 3D image. Since there are no blobs associated with the vertices on the Steiner-tree inspired graph, the 2D pixels that are close to a projected 3D point are directly saved to form the association. If no 2D points are found to be associated with a particular 3D point in all three views, a virtual association from the projection of the 3D point is created as a regularization in the fit.

The associations that have been formed are further examined. Only 2D pixels that are not associated with known non-functional channels and those with reconstructed charge higher than a threshold (2000 electrons as the default) are used during the examination. For any given view, the average location of the eligible 2D pixels is checked against the initial 2D projection of the 3D point. If the distance is larger than 75% of the position spread and the number of eligible 2D pixels is small compared to the possible number of 2D pixels, the established association is replaced by a virtual association to avoid the bias in the trajectory fit near non-functional channels. If a 2D pixel is associated among multiple 3D candidate points, its charge is equally distributed amongst the 3D points.

Appendix B: Stopped muon examples

In this appendix, we show several representative STM examples with difficult topologies or unusual dQ/dx distributions, and certain neutrino interactions that could be mis-identified as an STM.

Figure 26 shows a tagged up-going STM that enters from the bottom of the detector. The black curve is the fitted dQ/dx , and the blue curve is the reduced chi-squared (χ^2/ndf) value comparing the predicted and measured charge from each 2D pixel. This track is clearly not a cosmic-ray muon which would enter the detector from the top or side. However, a clear rise in dQ/dx near the stopping point can be seen. This track originates from a $\nu_\mu CC$ interaction outside the TPC active volume.

Only the muon enters the active TPC and is seen by the detector.

A similar example is shown in Fig. 27. This track enters the detector from the cathode plane and travels toward the top of the detector. The angle of the track is not consistent with that of a cosmic-ray muon. However, a clear rise in dQ/dx near the stopping point can be seen. This track, which also should originate from a $\nu_\mu CC$ interaction outside the TPC active volume, is tagged as an STM background. Note that similarly, a $\nu_\mu CC$ interaction can be tagged as TGM if its neutrino interaction vertex is outside the active volume and only the muon goes through the detector.

Figure 28 shows an example of an STM with a Michel electron attached to the end. This track enters from the anode plane. The stopped muon is quite short with about 23 cm length. The Michel electron is traveling vertically down leading to a very compact view in the collection W plane. The decay of the STM to a Michel electron (at ~ 23 cm) can be clearly seen in the dQ/dx distribution. The rise of dQ/dx before 23 cm is properly tagged by the STM tagger, and the residual dQ/dx is consistent with that of the Michel electron topology.

Figure 29 shows another example of an STM with a Michel electron attached to the end. The rise of dQ/dx before 256 cm is smaller compared to that in Fig. 26, but the residual track is consistent with a Michel electron. The algorithm discussed in Sec. VC successfully tags this event as an STM background by considering the possibility of a muon decaying in flight.

Similarly to the TGM tagger described in Sec. VB, simplified pattern recognition algorithms are applied in the STM tagger to protect against neutrino interactions that may mimic STMs. Most neutrino interactions result in multiple tracks and can be effectively removed by detecting a large angle deflection. For single-track-like neutrino events, Figure 30 shows an example neutrino interaction candidate. At the identified end point (kink) of the track, there is a very sharp rise in dQ/dx . Such a sharp rise is not consistent with the expectation for an STM. Instead, this should be the vertex of the neutrino interaction, and the high dQ/dx comes from a very short recoil proton or nucleus. A dedicated algorithm is developed to identify these neutrino interaction candidates based on the shape of the dQ/dx of the main track and the length and dQ/dx of the residual track.

Figure 31 shows another neutrino interaction example. There is a rise in dQ/dx near the stopping point tagged by the STM evaluation algorithm described in Sec. VC, partially because of the dip in dQ/dx in the region just before the stopping point. On the other hand, a long delta ray is identified as a separated track candidate along the main track. The direction of the delta ray with respect to the main track is used to determine the direction of the track. Since the track direction is not consistent with that of an incoming STM, this event is successfully tagged as a neutrino interaction.

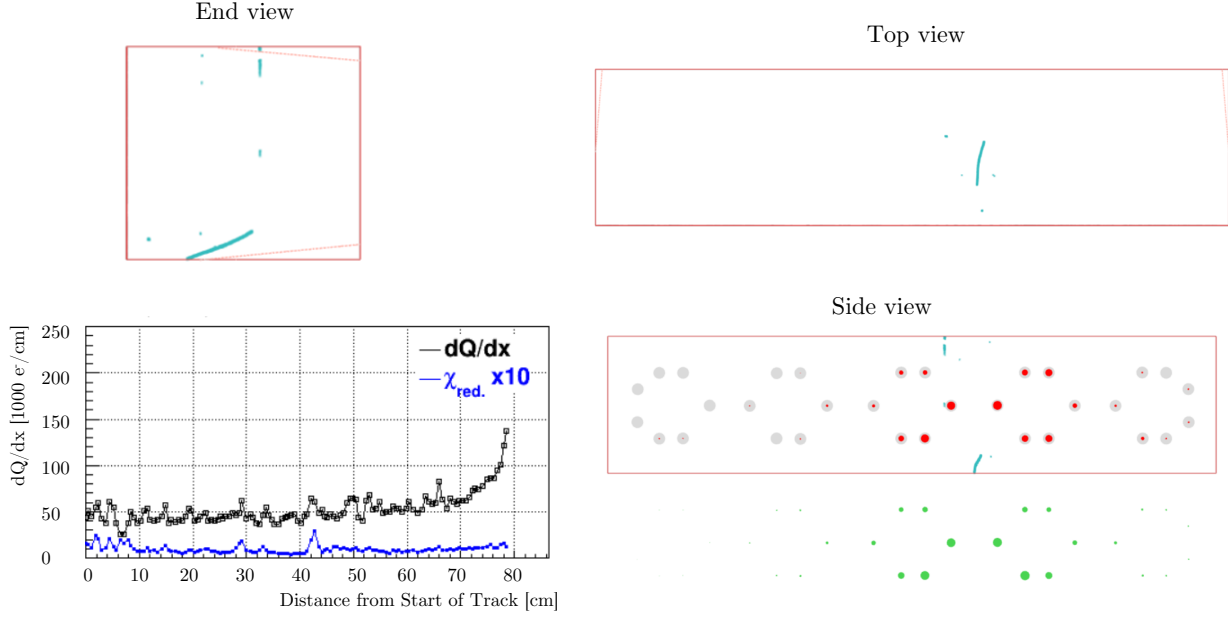


FIG. 26. An STM candidate with a extreme angle.

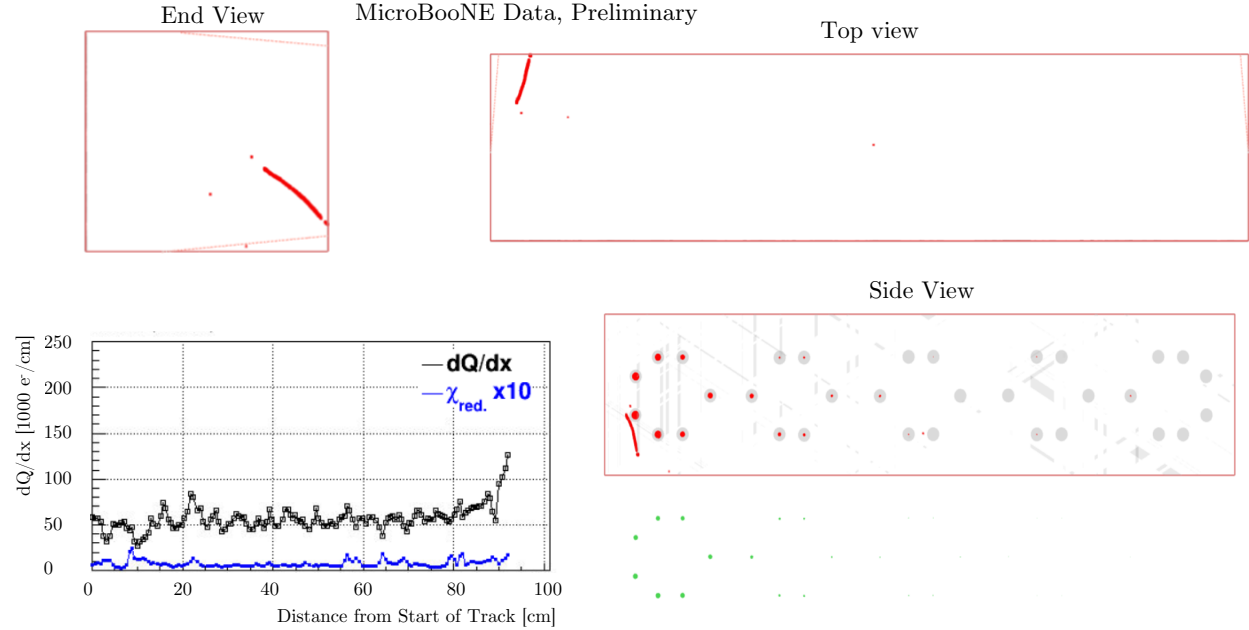


FIG. 27. An STM candidate with a extreme angle.

[1] C. Rubbia (1977), eERN-EP/77-08.
 [2] H. H. Chen, P. E. Condon, B. C. Barish, and F. J. Sciulli (1976), fERMILAB-PROPOSAL-0496.
 [3] W. J. Willis and V. Radeka, Nuclear Instruments and Methods **120**, 221 (1974).
 [4] D. R. Nygren, 1974 PEP summer study, eConf **C740805**, 58 (PEP-0144).
 [5] S. Amerio *et al.* (ICARUS), Nucl.Instrum.Meth. **A527**, 329 (2004).
 [6] C. Anderson *et al.* (ArgoNeuT), JINST **7**, P10019.

MicroBooNE Data, Preliminary

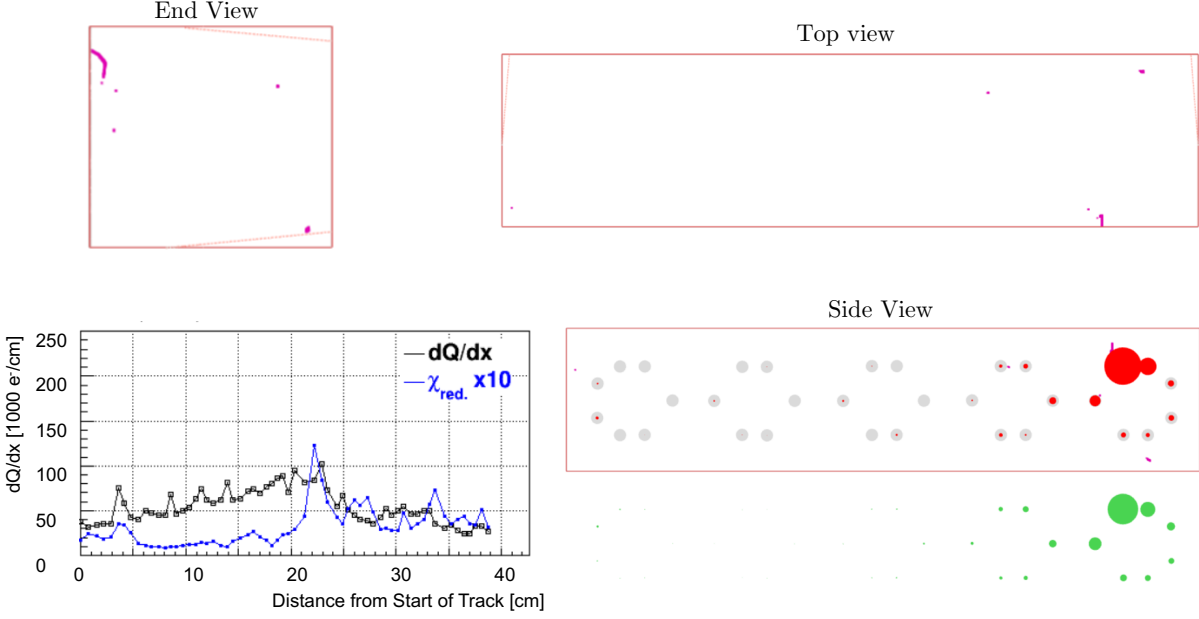


FIG. 28. An STM candidate with a short stopped muon track following by a Michel electron.

MicroBooNE Data, Preliminary

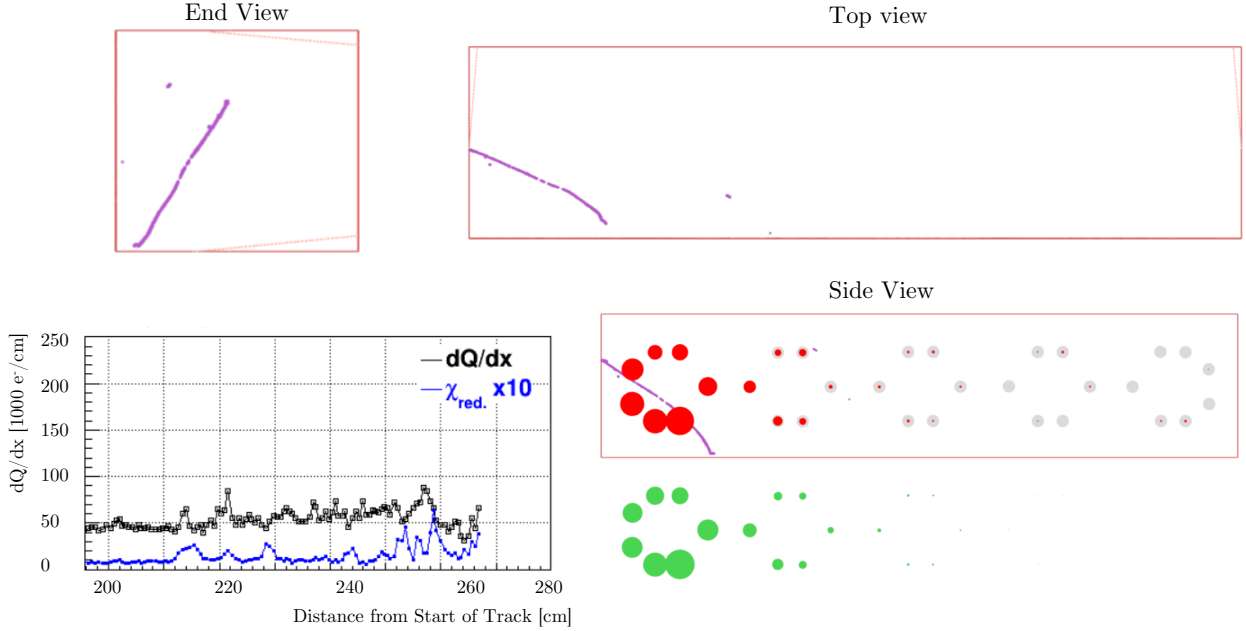


FIG. 29. An STM candidate with a small rise near the end.

[7] R. Acciarri *et al.* (MicroBooNE), JINST **12** (02), P02017, arXiv:1612.05824 [physics.ins-det].

[8] I. Badhrees *et al.*, *Position sensitive detectors. Proceedings, 9th International Conference, PSD9, Aberystwyth, UK, September 12-16, 2011*, JINST **7**, C02011.

[9] B. Bhandari *et al.* (CAPTAIN), Phys. Rev. Lett. **123**, 042502 (2019), arXiv:1903.05276 [hep-ex].

[10] A. Hahn, M. Adamowski, D. Montanari, B. Norris, J. Reichenbacher, R. Rucinski, J. Stewart, and T. Tope (LBNE), in *Proceedings, 21st Symposium on Room-Temperature Semiconductor X-ray and Gamma-ray Detectors (RTSD 2014): Seattle, WA, USA, November 8-15, 2014* (2016) p. 7431158.

[11] F. Cavanna, M. Kordosky, J. Raaf, and B. Rebel (LAr-

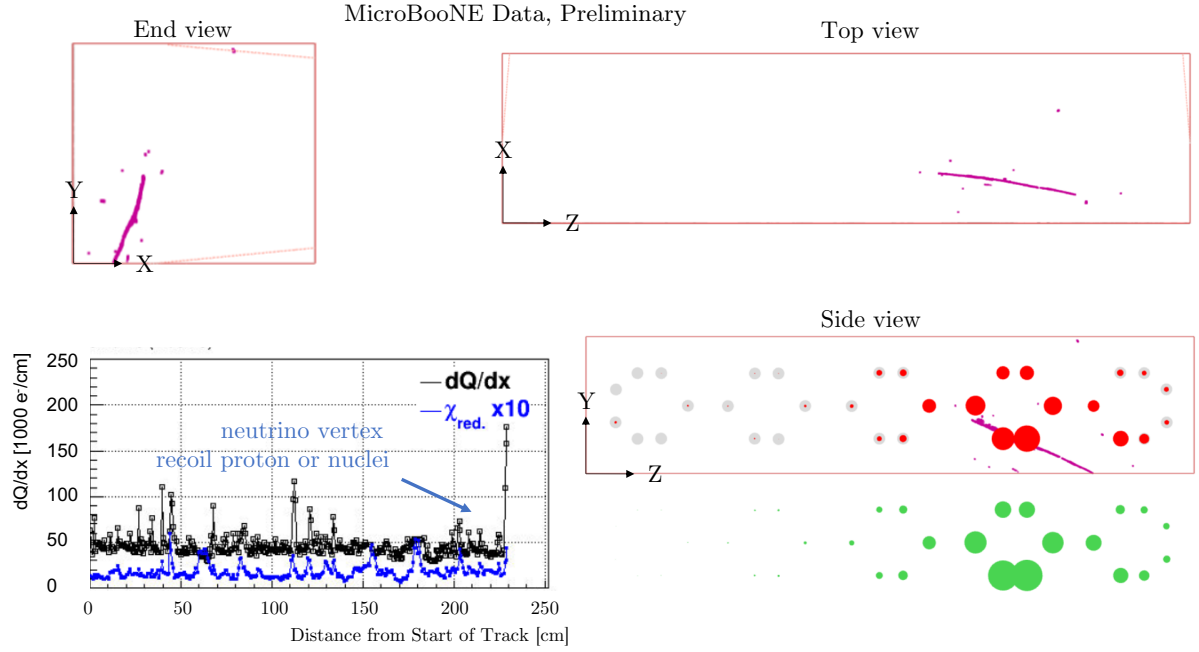


FIG. 30. A neutrino interaction candidate with a very high dQ/dx near the neutrino vertex. The sharp rise of dQ/dx (black line) near the end of track trajectory is presumably the result of a recoil proton or nucleus (bottom left panel).

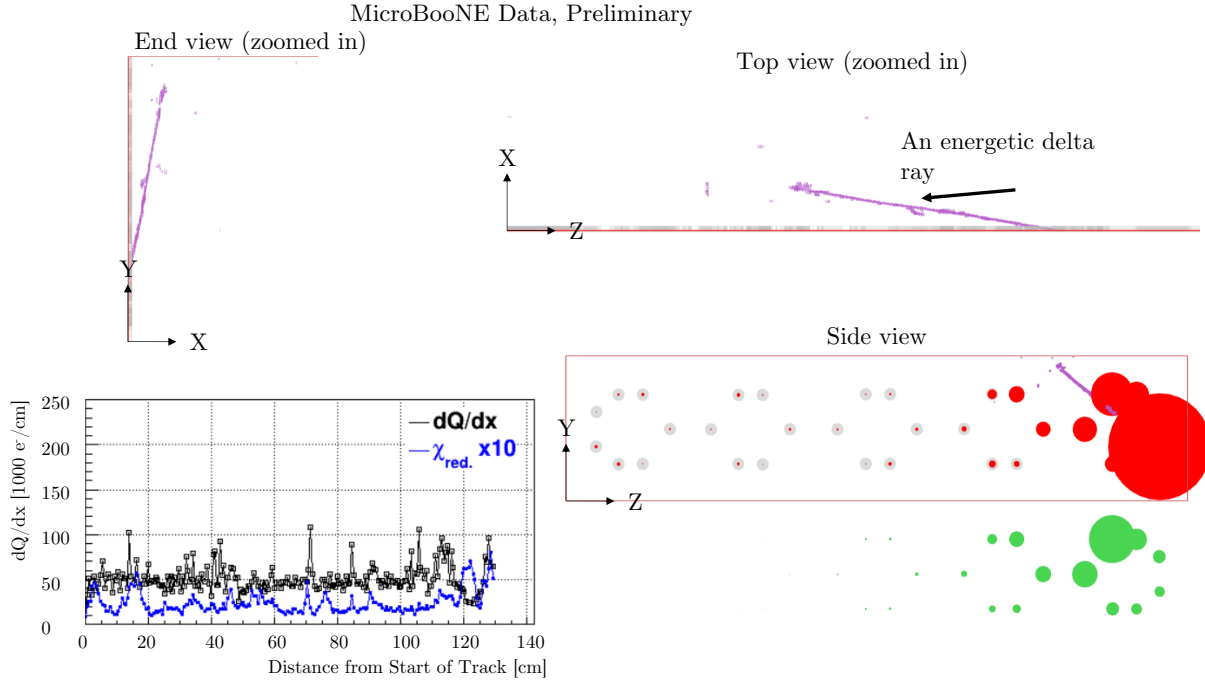


FIG. 31. A neutrino interaction candidate with an energetic delta ray. The track direction is obvious after taking into account the direction of the energetic delta ray. There is a rise in dQ/dx near the stopping point tagged by the STM evaluation algorithm described in Sec. V C. This rise is partially because of the dip in dQ/dx in the region just before the stopping point.

- IAT), (2014), arXiv:1406.5560 [physics.ins-det].
- [12] B. Abi *et al.* (DUNE), (2017), arXiv:1706.07081 [physics.ins-det].
- [13] F. Cavanna, A. Ereditato, and B. T. Fleming, Nucl. Instrum. Meth. **A907**, 1 (2018).

- [14] A. A. Aguilar-Arevalo *et al.* (MiniBooNE) (2012) arXiv:1207.4809 [hep-ex].
- [15] P. Abratenko *et al.* (MicroBooNE), Phys. Rev. Lett. **123**, 131801 (2019), arXiv:1905.09694 [hep-ex].
- [16] C. Adams *et al.* (MicroBooNE), Phys. Rev. **D99**, 091102

- (2019), arXiv:1811.02700 [hep-ex].
- [17] M. Antonello *et al.* (MicroBooNE, LAr1-ND, ICARUS-WA104), arXiv:1503.01520 (2015), arXiv:1503.01520 [physics.ins-det].
- [18] P. A. Machado, O. Palamara, and D. W. Schmitz, *Ann. Rev. Nucl. Part. Sci.* **69** (2019), arXiv:1903.04608 [hep-ex].
- [19] B. Abi *et al.* (DUNE), (2020), arXiv:2002.02967 [physics.ins-det].
- [20] B. Abi *et al.* (DUNE), (2020), arXiv:2002.03005 [hep-ex].
- [21] X. Qian and P. Vogel, *Prog. Part. Nucl. Phys.* **83**, 1 (2015), arXiv:1505.01891 [hep-ex].
- [22] X. Qian, C. Zhang, B. Viren, and M. Diwan, *JINST* **13** (05), P05032, arXiv:1803.04850 [physics.ins-det].
- [23] T. Briese *et al.*, *JINST* **8**, T07005, arXiv:1304.0821 [physics.ins-det].
- [24] A. A. Aguilar-Arevalo *et al.* (MiniBooNE), *Phys. Rev. D.* **79**, 072002 (2009), arXiv:0806.1449 [hep-ex].
- [25] R. Acciarri *et al.* (MicroBooNE), *JINST* **12** (12), P12030, arXiv:1707.09903 [hep-ex].
- [26] C. Adams *et al.* (MicroBooNE), *Eur. Phys. J.* **C79**, 248 (2019), arXiv:1805.06887 [hep-ex].
- [27] C. Adams *et al.* (MicroBooNE), *Eur. Phys. J.* **C79**, 673 (2019), arXiv:1812.05679 [physics.ins-det].
- [28] P. Abratenko *et al.* (MicroBooNE), *Phys. Rev. Lett.* **123**, 131801 (2019), arXiv:1905.09694 [hep-ex].
- [29] P. Adamson *et al.*, *Nucl. Instrum. Meth.* **A806**, 279 (2016), arXiv:1507.06690 [physics.acc-ph].
- [30] M. Del Tutto, in *Proceedings, Meeting of the APS Division of Particles and Fields (DPF 2017): Fermilab, Batavia, Illinois, USA, July 31 - August 4, 2017* (2017) arXiv:1709.10120 [physics.pop-ph].
- [31] Y. Li *et al.*, *Nucl. Instrum. Meth.* **A816**, 160 (2016), arXiv:1508.07059 [physics.ins-det].
- [32] V. Radeka *et al.*, *Giant liquid argon charge imaging experiment. Proceedings, 1st International Workshop, GLA2010, Tsukuba, Japan, March 29-31, 2010*, *J. Phys. Conf. Ser.* **308**, 012021 (2011).
- [33] R. Acciarri *et al.* (MicroBooNE), *JINST* **12** (08), P08003, arXiv:1705.07341 [physics.ins-det].
- [34] Wire-Cell 3D imaging, clustering and charge-light matching in MicroBooNE.
- [35] C. Adams *et al.* (MicroBooNE), *JINST* **13** (07), P07006, arXiv:1802.08709 [physics.ins-det].
- [36] C. Adams *et al.* (MicroBooNE), *JINST* **13** (07), P07007, arXiv:1804.02583 [physics.ins-det].
- [37] B. Baller, *JINST* **12** (07), P07010, arXiv:1703.04024 [physics.ins-det].
- [38] E. J. Candès, J. K. Romberg, and T. Tao, *Communications on Pure and Applied Mathematics* **59**, 1207 (2006), math/0503066.
- [39] P. Adamson *et al.* (NOvA), *Phys. Rev.* **D93**, 051104 (2016), arXiv:1601.05037 [hep-ex].
- [40] L. Aliaga *et al.* (MINERvA), *Nucl. Instrum. Meth.* **A743**, 130 (2014), arXiv:1305.5199 [physics.ins-det].
- [41] D. G. Michael *et al.* (MINOS), *Nucl. Instrum. Meth.* **A596**, 190 (2008), arXiv:0805.3170 [physics.ins-det].
- [42] M. Antonello *et al.* (ICARUS), *JINST* **12** (04), P04010, arXiv:1612.07715 [physics.ins-det].
- [43] P. Abratenko *et al.* (MicroBooNE), *JINST* **12** (10), P10010, arXiv:1703.06187 [physics.ins-det].
- [44] R. E. Kalman, *Journal of Basic Engineering* **82**, 35 (1960).
- [45] M. Antonello *et al.*, *Adv. High Energy Phys.* **2013**, 260820 (2013), arXiv:1210.5089 [physics.ins-det].
- [46] Biconjugate gradient stablized method (BiCGSTAB), https://eigen.tuxfamily.org/dox/classEigen_1_1BiCGSTAB.html.
- [47] <https://lar.bnl.gov/properties/spacecharge.html>.
- [48] C. Adams *et al.* (MicroBooNE), (2019), arXiv:1910.01430 [physics.ins-det].
- [49] PSTAR at NIST: <https://physics.nist.gov/PhysRefData/Star/Text/PSTAR.html>.
- [50] R. Acciarri *et al.* (ArgoNeuT), *JINST* **8**, P08005, arXiv:1306.1712 [physics.ins-det].
- [51] C. Adams *et al.* (MicroBooNE), (2019), arXiv:1907.11736 [physics.ins-det].
- [52] R. Acciarri *et al.* (MicroBooNE), *Eur. Phys. J.* **C78**, 82 (2018), arXiv:1708.03135 [hep-ex].
- [53] R. Acciarri *et al.* (MicroBooNE), *JINST* **12** (03), P03011, arXiv:1611.05531 [physics.ins-det].
- [54] C. Adams *et al.* (MicroBooNE), *Phys. Rev.* **D99**, 092001 (2019), arXiv:1808.07269 [hep-ex].
- [55] C. Adams *et al.* (MicroBooNE), (2019), arXiv:1910.02166 [hep-ex].
- [56] (), graph theory operation: Dijkstra's Shortest Path https://www.boost.org/doc/libs/1_41_0/libs/graph/doc/dijkstra_shortest_paths.html.
- [57] Steiner Tree Greedy Algorithm in Practical Approximation Algorithms Library, <http://paal.mimuw.edu.pl/docs/index.html>.
- [58] (), graph theory operation: connected component https://www.boost.org/doc/libs/1_68_0/libs/graph/doc/connected_components.html.